Hsu, Brian, Smith, Nathan, Goldberg, Jared A., Bostroem, K. Azalee, Hosseinzadeh, Griffin, Sand, David J., Pearson, Jeniveve, Hiramatsu, Daichi, Andrews, Jennifer E., Beasor, Emma R., Dong, Yize, Farah, Joseph, Galbany, Lluís, Gomez, Sebastian, Padilla Gonzalez, Estefania, Gutiérrez, Claudia P., Howell, D. Andrew, Könyves-Tóth, Réka, McCully, Curtis, Newsome, Megan, Shrestha, Manisha, Terreran, Giacomo, Villar, V. Ashley and Wang, Xiaofeng

One Year of SN 2023ixf: Breaking through the Degenerate Parameter Space in Light-curve Models with Pulsating Progenitors

https://researchonline.ljmu.ac.uk/id/eprint/27095/

Article

Citation (please note it is advisable to refer to the publisher's version if you intend to cite from this work)

Hsu, Brian ORCID logoORCID: https://orcid.org/0000-0002-9454-1742, Smith, Nathan ORCID logoORCID: https://orcid.org/0000-0001-5510-2424, Goldberg, Jared A. ORCID logoORCID: https://orcid.org/0000-0003-1012-3031, Bostroem, K. Azalee ORCID logoORCID: https://orcid.org/0000-0002-

The Astrophysical Journal, 990:148 (16pp), 2025 September 10 https://doi.org/10.3847/1538-4357/adf222

One Year of SN 2023ixf: Breaking through the Degenerate Parameter Space in Light-curve Models with Pulsating Progenitors

Brian Hsu[1], Nathan Smith[1], Jared A. Goldberg[2], K. Azalee Bostroem[1], Griffin Hosseinzadeh[3], David J. Sand[1], Jeniveve Pearson[1], Daichi Hiramatsu[4,5], Jennifer E. Andrews[6], Emma R. Beasor[7], Yize Dong (董一泽)[4,5], Joseph Farah[8,9], Lluís Galbany[10,11], Sebastian Gomez[4], Estefania Padilla Gonzalez[8,9], Claudia P. Gutiérrez[10,11], D. Andrew Howell[8,9], Réka Könyves-Tóth[12,13], Curtis McCully[8], Megan Newsome[8,9], Manisha Shrestha[1], Giacomo Terreran[8], V. Ashley Villar[4,5], and Xiaofeng Wang[14]

[1] Steward Observatory, University of Arizona, 933 North Cherry Avenue, Tucson, AZ 85721-0065, USA; bhsu@arizona.edu
[2] Center for Computational Astrophysics, Flatiron Institute, 162 5th Avenue, New York, NY 10010-5902, USA
[3] Department of Astronomy & Astrophysics, University of California, San Diego, 9500 Gilman Drive, MC 0424, La Jolla, CA 92093-0424, USA
[4] Center for Astrophysics | Harvard & Smithsonian, 60 Garden Street, Cambridge, MA 02138-1516, USA
[5] The NSF AI Institute for Artificial Intelligence and Fundamental Interactions, USA
[6] Gemini Observatory, 670 North A'ohoku Place, Hilo, HI 96720-2700, USA
[7] Astrophysics Research Institute, Liverpool John Moores University, 146 Brownlow Hill, Liverpool, L3 5RF, UK
[8] Las Cumbres Observatory, 6740 Cortona Drive, Suite 102, Goleta, CA 93117-5575, USA
[9] Department of Physics, University of California, Santa Barbara, CA 93106-9530, USA
[10] Institute of Space Sciences (ICE, CSIC), Campus UAB, Carrerde Can Magrans, s/n, E-08193 Barcelona, Spain
[11] Institut d'Estudis Espacials de Catalunya (IEEC), Edifici RDIT, Campus UPC, 08860 Castelldefels (Barcelona), Spain
[12] Konkoly Observatory, HUN-REN Research Centre for Astronomy and Earth Sciences (MTA Centre of Excellence), Konkoly Thege Miklós út 15-17, Budapest, 1121, Hungary
[13] Department of Experimental Physics, Institute of Physics, University of Szeged, Dóm tér 9, Szeged, 6720, Hungary
[14] Physics Department and Tsinghua Center for Astrophysics, Tsinghua University, Beijing, 100084, People's Republic of China

Received 2024 August 14; revised 2025 July 9; accepted 2025 July 17; published 2025 September 4

Abstract

We present and analyze the extensive optical broadband photometry of the Type II SN 2023ixf up to 1 yr after explosion. We find that, when compared to two preexisting model grids, the bolometric light curve is consistent with drastically different combinations of progenitor and explosion properties. This may be an effect of known degeneracies in Type IIP light-curve models. We independently compute a large grid of `MESA+STELLA` single-star progenitor and light-curve models with various zero-age main-sequence masses, mass-loss efficiencies, and convective efficiencies. Using the observed progenitor variability as an additional constraint, we select stellar models consistent with the pulsation period and explode them according to previously established scaling laws to match plateau properties. Our hydrodynamic modeling indicates that SN 2023ixf is most consistent with a moderate-energy ($E_{\mathrm{exp}} \approx 7 \times 10^{50}$ erg) explosion of an initially high-mass red supergiant progenitor ($\gtrsim 16.5\,M_\odot$) that lost a significant amount of mass in its prior evolution, leaving a low-mass hydrogen envelope ($\lesssim 3\,M_\odot$) at the time of explosion, with a radius $\gtrsim 950\,R_\odot$ and a synthesized ^{56}Ni mass of $\approx 0.068\,M_\odot$. We posit that previous mass transfer in a binary system may have stripped the envelope of SN 2023ixf's progenitor. The analysis method with pulsation period presented in this work offers a way to break degeneracies in light-curve modeling in the future, particularly with the upcoming Vera C. Rubin Observatory Legacy Survey of Space and Time, when a record of progenitor variability will be more common.

Unified Astronomy Thesaurus concepts: Core-collapse supernovae (304); Supernovae (1668); Type II supernovae (1731); Massive stars (732); Red supergiant stars (1375); Stellar mass loss (1613)

Materials only available in the online version of record: data behind figure

1. Introduction

Type II supernovae (SNe II) are hydrogen-rich core-collapse supernovae (CCSNe) that are thought to mark the violent deaths of massive stars ($\gtrsim 8\,M_\odot$; S. E. Woosley & T. A. Weaver 1986). Those with a plateau shape in the light curves (SNe IIP) are the most common variety of massive-star explosions, representing about half of all CCSNe (N. Smith et al. 2011). Their progenitors have been confirmed to be red supergiants (RSGs) by pre-explosion detections, with zero-age main-sequence (ZAMS) masses in the range of $M_{\mathrm{ZAMS}} \approx 8$–$20\,M_\odot$ (e.g., S. D. Van Dyk et al. 2003, 2012, 2023; W. Li et al. 2006; S. J. Smartt 2009, 2015; B. Davies & E. R. Beasor 2020). Even with direct detections of the progenitor star in pre-explosion imaging, inferring the initial mass of the exploding star is subject to significant uncertainty, leading to much debate about the initial masses of SNe IIP (S. J. Smartt 2015; B. Davies & E. R. Beasor 2018, 2020). Clues to the star's mass may also be inferred from the shape of the plateau light curve, since this shape is mediated by the recombination of the hydrogen envelope (R. P. Kirshner & J. Kwan 1975; T. Shigeyama & K. Nomoto 1990; N. N. Chugai 1991; D. V. Popov 1993; V. P. Utrobin & N. N. Chugai 2005). This is complicated, however, by the fact that the light-curve shape depends on other factors like the explosion energy and progenitor radius (I. I. Litvinova & D. K. Nadezhin 1983; N. N. Chugai 1991;

D. Kasen & S. E. Woosley 2009; L. Dessart et al. 2013; O. Pejcha & J. L. Prieto 2015; T. Sukhbold et al. 2016; J. A. Goldberg et al. 2019; L. Martinez et al. 2022b).

Extensive photometric and spectroscopic follow-up at multiple wavelengths over the duration of SN II light curves can help probe the underlying physics during different phases of their evolution (e.g., C. Fransson 1984; L. Dessart & D. J. Hillier 2005, 2006, 2008; L. Dessart et al. 2013; D. J. Hillier & L. Dessart 2019; J. E. Jencson et al. 2019; A. Kozyreva et al. 2019, 2020; L. Dessart & W. V. Jacobson-Galán 2023; L. Dessart 2025). In particular, when SNe II are discovered very soon after explosion, early observations offer unique insight into the explosion geometry, surrounding environments, and mass loss during the final years of the massive star's life (e.g., E. Baron et al. 2000; P. J. Brown et al. 2007; N. Smith 2014; L. Dessart & D. J. Hillier 2022; W. V. Jacobson-Galán et al. 2022, 2024; K. A. Bostroem et al. 2023a, 2023b; G. Li et al. 2024; M. Shrestha et al. 2024a, 2024b).

Spectroscopic observations of some SNe II within a few days of explosion have revealed narrow emission features from slow circumstellar material (CSM) with high-ionization states (e.g., V. S. Niemela et al. 1985; P. M. Garnavich & H. B. Ann 1994; R. M. Quimby et al. 2007; A. Gal-Yam et al. 2014; J. H. Groh 2014; I. Shivvers et al. 2015; N. Smith et al. 2015; D. Khazov et al. 2016; O. Yaron et al. 2017; C. Bullivant et al. 2018; L. Tartaglia et al. 2021; R. J. Bruch et al. 2021, 2023; J. Zhang et al. 2023; J. E. Andrews et al. 2024; M. Shrestha et al. 2024a, 2024b). Several SNe II have also exhibited light-curve excess above the canonical shock-cooling model (e.g., G. Hosseinzadeh et al. 2018, 2022; J. E. Andrews et al. 2019, 2024; Y. Dong et al. 2021; L. Tartaglia et al. 2021; J. Pearson et al. 2023; M. Shrestha et al. 2024a, 2024b). Combined with recent efforts of detailed hydrodynamic and radiative transfer modeling involving dense CSM (V. Morozova et al. 2017, 2018; I. Boian & J. H. Groh 2019; L. Dessart & D. J. Hillier 2022; L. Dessart & W. V. Jacobson-Galán 2023; T. J. Moriya et al. 2023), observations and theory alike seem to suggest that a significant portion of SN II progenitors were enshrouded in CSM shells or inflated envelopes (e.g., F. Förster et al. 2018; V. Morozova et al. 2018; R. J. Bruch et al. 2023; W. V. Jacobson-Galán et al. 2024). If unbound and sustained, the formation of this dense CSM requires an enhanced mass-loss rate $\sim 10^{-4}$–$10^{-2}\,M_{\odot}$ yr^{-1} in the months to years prior to the onset of core collapse, which is much higher than values expected for normal stellar winds of RSGs (e.g., N. Mauron & E. Josselin 2011; E. R. Beasor & B. Davies 2018; E. R. Beasor et al. 2020; E. R. Beasor & N. Smith 2022). While the exact nature of such an intense mass-loss episode is still unclear, several mechanisms have been proposed, including, but not limited to, late-phase nuclear burning instabilities (W. D. Arnett & C. Meakin 2011; N. Smith & W. D. Arnett 2014; S. E. Woosley & A. Heger 2015), wave-driven mass loss (E. Quataert & J. Shiode 2012; J. H. Shiode et al. 2013; J. H. Shiode & E. Quataert 2014; J. Fuller 2017; S. Wu & J. Fuller 2021; S. C. Wu & J. Fuller 2022), binary interaction (N. Smith & W. D. Arnett 2014), atmospheric shocks (J. Fuller & D. Tsuna 2024), and pulsation-driven superwinds (S.-C. Yoon & M. Cantiello 2010).

Recently, SN 2023ixf provided another clear case of an SN II progenitor surrounded by dense CSM structures, since it was discovered very early after explosion (G. Hosseinzadeh et al. 2023b; G. Li et al. 2024) and showed short-lived narrow emission lines in its early spectra (K. A. Bostroem et al. 2023b; D. Hiramatsu et al. 2023; W. V. Jacobson-Galán et al. 2023; N. Smith et al. 2023; A. Singh et al. 2024; E. A. Zimmerman et al. 2024). SN 2023ixf is an SN II (D. A. Perley et al. 2023) discovered on 2023 May 19 17:27:15.00 UT (K. Itagaki 2023) in the Pinwheel Galaxy. The earliest observation of this SN can be traced back to about 0.9 days before discovery, corresponding to a phase at about 1 hr after explosion (G. Li et al. 2024). Its proximity to Earth offers an unprecedented opportunity to study the late-stage evolution of RSGs and physics pertaining to SNe II encoded in its extensively sampled light curve across the electromagnetic spectrum. Analyses of both the early light curve and the spectral series from radio to γ-ray wavelengths all have indicated the presence of dense CSM surrounding its RSG progenitor (E. Berger et al. 2023; K. A. Bostroem et al. 2023a; B. W. Grefenstette et al. 2023; D. Hiramatsu et al. 2023; W. V. Jacobson-Galán et al. 2023; D. Matthews et al. 2023; N. Smith et al. 2023; R. S. Teja et al. 2023; M. Yamanaka et al. 2023; J. Zhang et al. 2023; P. Chandra et al. 2024; L. Martinez et al. 2024; S. Panjkov et al. 2024). This was further supported by optical spectropolarimetry observations (S. S. Vasylyev et al. 2023; A. Singh et al. 2024; M. Shrestha et al. 2025) and the evolution of shock breakout emission (G. Li et al. 2024), suggesting that either the CSM or the explosion was asymmetric. The inferred mass-loss rate from these studies probed a wide range of 10^{-6}–$10^{-2}\,M_{\odot}$ yr^{-1} at various layers of the CSM, indicating a time-variable mass-loss history.

Using pre-explosion images from the Hubble Space Telescope, Spitzer Space Telescope, and various ground-based facilities, the properties of the candidate RSG progenitor of SN 2023ixf have also been estimated. In particular, the ZAMS masses estimated independently from spectral energy density (SED) fitting, comparison with single-star evolutionary tracks, environmental studies in the vicinity of the SN, and analysis of infrared (IR) variability collectively yield a large range of $M_{\mathrm{ZAMS}} \approx 8$–$20\,M_{\odot}$ (J. E. Jencson et al. 2023; Z. Niu et al. 2023; J. L. Pledger & M. M. Shara 2023; M. D. Soraisam et al. 2023; J. M. M. Neustadt et al. 2024; Y.-J. Qin et al. 2024; S. D. Van Dyk et al. 2024; D. Xiang et al. 2024). Given the uncertainties in both the progenitor's inferred mass-loss rate and initial mass, it is useful to derive the progenitor properties using an alternative method. For example, M. C. Bersten et al. (2024) compared the bolometric light curve and expansion velocity evolution of SN 2023ixf to hydrodynamic models. They found a model with an initial mass of $12\,M_{\odot}$, an explosion energy of 1.2×10^{51} erg, and a synthesized ^{56}Ni mass of $0.05\,M_{\odot}$ to be compatible with the observed luminosity evolution. Similar low-mass progenitor models were also favored by T. J. Moriya & A. Singh (2024) and A. Singh et al. (2024) based on light-curve fitting, and by L. Ferrari et al. (2024) based on nebular-phase spectroscopy.

In this paper, we present new observations and an independent analysis of the densely sampled optical light curves of SN 2023ixf. The optical photometry presented in this paper has a $\sim$2 day cadence in seven bands, extending up to a year after discovery. We give a description of the observations and the data reduction process in Section 2, followed by the methodologies used to calculate the bolometric light curve, plateau properties, and radioactive tail properties of SN 2023ixf. Section 3 compares our observations to publicly available hydrodynamic model grids and Section 4 presents our independent modeling of the bolometric and multiband light curves. We additionally include the observed RSG variability to aid model selection, and this reveals evidence for a small H-rich envelope mass and high ZAMS mass for SN 2023ixf's progenitor. As such, we discuss the possible formation channel and implications for the progenitor of SN 2023ixf in Section 5. Finally, we summarize our findings and draw conclusions in Section 6.

2. Observations and Initial Analysis

2.1. Photometry and Reductions

Following the discovery of SN 2023ixf by K. Itagaki (2023), continuous photometric monitoring of the Pinwheel Galaxy was carried out using the Sinistro cameras on the Las Cumbres Observatory (LCO) robotic 1 m telescopes (T. M. Brown et al. 2013) at Teide Observatory (Canary Islands, Spain), McDonald Observatory (Texas, USA), and Haleakalā Observatory (Hawai'i, USA) as part of the Global Supernova Project collaboration (D. A. Howell & Global Supernova Project 2017). The $UBVgriz_s$ data were reduced using `lcogtsnpipe` (S. Valenti et al. 2016), a `PyRAF`-based image reduction pipeline that utilizes a standard point-spread function fitting procedure to measure instrumental magnitudes. *UBV* magnitudes were calibrated to stars in the L92 standard fields of A. U. Landolt (1983, 1992) observed on the same night with the same telescopes, *gri* magnitudes were calibrated to the AAVSO Photometric All-sky Survey (A. A. Henden et al. 2016) catalog, and z_s magnitudes were calibrated to the Sloan Digital Sky Survey (F. D. Albareti et al. 2017) catalog. The early photometry up to 2023 June 18 (MJD = 60113; 30 days after discovery) following the same reduction procedure has been presented in G. Hosseinzadeh et al. (2023b) and D. Hiramatsu et al. (2023).[15] All magnitudes are reported in the AB system and are available as data behind Figure 1.

The Pinwheel Galaxy has a luminosity distance of $d_L = 6.71 \pm 0.14$ Mpc ($\mu = 29.135 \pm 0.045$ mag; A. G. Riess et al. 2016), measured via the H. S. Leavitt (1908) law of Cepheid variables. The Milky Way reddening in the direction of SN 2023ixf is $E(B-V)_{\rm MW} = 0.0077$ mag (E. F. Schlafly & D. P. Finkbeiner 2011), and the host-galaxy extinction is $E(B-V)_{\rm host} = 0.031 \pm 0.006$ mag (M. Lundquist et al. 2023; N. Smith et al. 2023). We correct for both Galactic and host extinction using an E. L. Fitzpatrick (1999) extinction law with $R_V = 3.1$ and adopt MJD 60082.788 as the explosion date, following the analysis of G. Li et al. (2024).

2.2. Bolometric Light Curve

Even with the large set of optical photometry covering 3250–9740 Å presented in this work, A. Singh et al. (2024) showed that without ultraviolet (UV) and near-IR (NIR) coverage, the luminosity may be underestimated by a factor of up to ~10 during the first ~10 days and a factor of ~2 during the nebular phase of SN 2023ixf's evolution, respectively. Therefore, to allow for a more robust construction of the bolometric light curve that captures both early- and late-time behaviors, we include NIR and UV photometry from A. Singh et al. (2024) and E. A. Zimmerman et al. (2024). The NIR data contain *J*-, *H*-, and K_s-band photometry from various ground-based facilities, while the UV data contain *UVW*1, *UVM*2, and *UVW*2 photometry from the Ultraviolet Optical Telescope (UVOT; P. W. A. Roming et al. 2005) on board the Neil Gehrels Swift Observatory (N. Gehrels et al. 2004). The inclusion of UV and NIR photometry extends our spectral coverage to 0.16–2.35 μm. To fill in the gap in our LCO light curves from ~120 to 150 days after explosion, we also supplement our data with optical photometry from A. Singh et al. (2024). All supplemental photometry is shown in Figure 1 in different markers.

We first generate a UVOIR pseudo-bolometric light curve of SN 2023ixf up to ~150 days after explosion, corresponding to the phase where we have complete multiwavelength coverage from UV to NIR. To obtain observations at all intermediate epochs across all bands, we interpolate the multiband light curves using a low-order polynomial using `scipy` (P. Virtanen et al. 2020). Equipped with photometric measurements and interpolations in all available bands at all epochs, we convert the magnitudes to monochromatic fluxes at the mean wavelength of each filter using the transmission functions and magnitude zero-points. The pseudo-bolometric luminosity at each epoch is then calculated via a full integration of the monochromatic fluxes using the trapezoidal rule within the wavelength range. To account for magnitude uncertainties, we perform a Monte Carlo procedure by sampling a Gaussian distribution centered at the magnitude value with the magnitude uncertainty as one standard deviation. This procedure is done 10,000 times for each epoch, and we report the median and standard deviation as the corresponding pseudo-bolometric luminosity and uncertainty.

Next, to account for any potentially missing flux, we perform blackbody (BB) fits to the SEDs of SN 2023ixf to obtain the effective BB temperature ($T_{\rm BB}$) and photospheric radius ($R_{\rm BB}$) at each epoch using the `Python`-based Markov Chain Monte Carlo routine `emcee` (D. Foreman-Mackey et al. 2013), implemented in the Light Curve Fitting package (G. Hosseinzadeh et al. 2023a). Here, we follow the same fitting procedure in T. Faran et al. (2018) and L. Martinez et al. (2022a), where we remove bands that deviate more than 1σ from the best-fit BB model, either due to strong line emission (e.g., Hα for *r* band and NIR Ca II triplet for *z* band) or due to line-blanketing effects of iron-group elements. We then calculate additional UV and IR bolometric corrections at each epoch by extrapolating the best-fit BB spectrum from the *UW*2 band to $\lambda = 0$ Å and from the *K* band to infinity, respectively. The full bolometric light curve is then derived by summing the pseudo-bolometric light curve with the bolometric corrections. A similar Monte Carlo procedure is performed by sampling the posterior distributions of the BB fits to obtain uncertainty estimates.

The full evolution of photospheric temperature and radius is shown in Figure 2. Similar to previous studies (L. Martinez et al. 2024; A. Singh et al. 2024; E. A. Zimmerman et al. 2024), we find a steep increase in $T_{\rm BB}$ over the first ~5 days of SN 2023ixf's evolution. However, the peak temperature of ≈26,000 K we find is about ≈11,000 K lower. This is due to the fact that the early-time evolution of SN 2023ixf is driven by shock interaction with a dense CSM, which causes its spectrum to depart from a BB. Depending on the combination of bands used

---

[15] We independently reduce the early photometry to avoid introducing systematic uncertainties, which may lead to slight differences in the reported magnitudes compared to these previous studies.

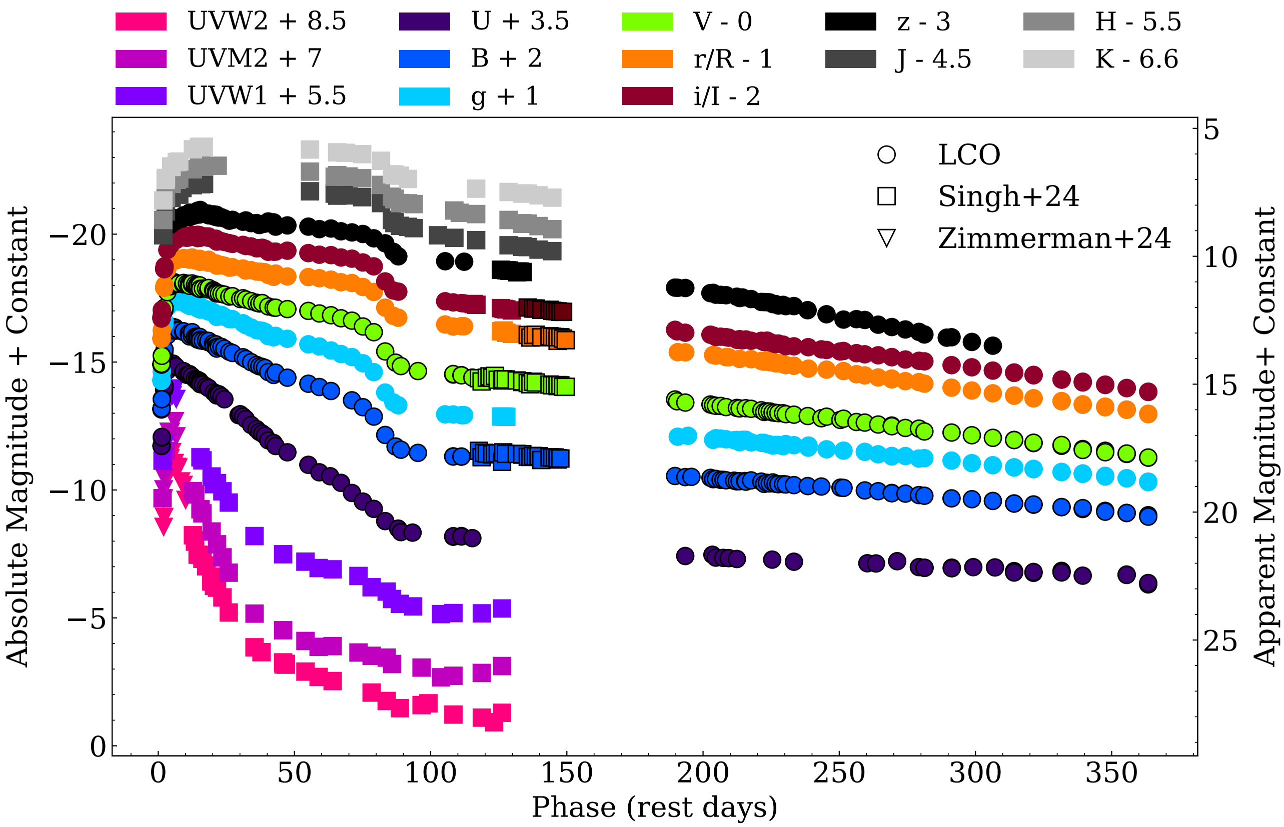

Figure 1. Multiband light curves of SN 2023ixf from LCO (circles) up to roughly 1 yr after discovery, supplemented with additional UV/optical/near-IR photometry from A. Singh et al. (2024, squares) and E. A. Zimmerman et al. (2024, triangles). All photometry has been corrected for Milky Way and host extinctions. The magnitude uncertainties ($\lesssim$0.1 mag) are smaller than the marker size.

(The data used to create this figure are available in the online article.)

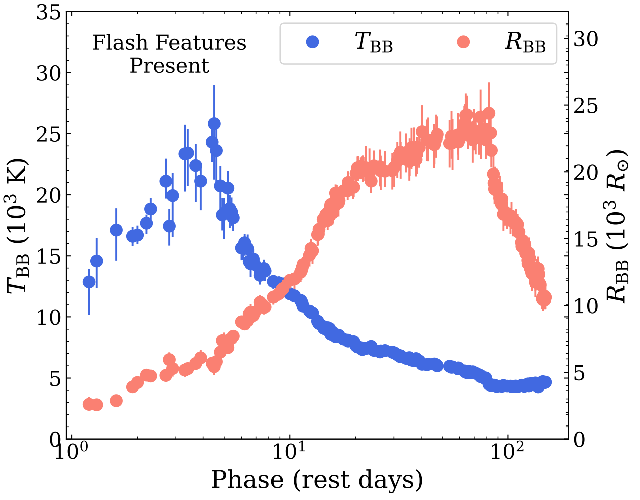

Figure 2. Evolution of photospheric temperature and radius of SN 2023ixf estimated from BB fits to the UVOIR multiband photometry. The region shaded in gray indicates phases where SN 2023ixf's evolution is dominated by energy from CSM interaction (up to ∼8 days after explosion) based on the epoch of disappearance of narrow line features in A. Singh et al. (2024).

(UV+optical versus optical+NIR), the inferred temperature can vary up to ≈10,000 K, which translates to a factor of ∼2 in the extrapolated bolometric luminosity. Nevertheless, our temperature evolution is consistent with the spectral BB fits in W. Zheng et al. (2025). We do caution that once SN 2023ixf enters the nebular phase, the ejecta become optically thin and emission dominated, and there may be late-time CSM interaction (K. A. Bostroem et al. 2024; A. Singh et al. 2024; G. Folatelli et al. 2025; A. Kumar et al. 2025) in addition to ^{56}Ni decay. In this case, a BB model cannot accurately capture the continuum flux at longer wavelengths. However, as shown by L. Martinez et al. (2022a), even though BB fits may not be physical during the nebular phase, the bolometric corrections calculated using BB extrapolations are representative of the missing flux at mid-IR wavelengths.

As the goal of this work is to constrain the progenitor and explosion characteristics of SN 2023ixf, which depend primarily on properties during the plateau phase and the radioactive tail, the uncertainty in bolometric luminosity during the CSM interaction phase should not affect the remainder of our analysis.

2.3. Measuring Plateau Duration and Nickel Mass

We estimate the plateau duration t_p following S. Valenti et al. (2016),[16] fitting the functional form $y(t) = V_{\rm mag}$ to the V-band light curve and $y(t) = \log_{10}(L_{\rm bol})$ to the bolometric light curve around the fall from the plateau:

$$y(t) = \frac{-A_0}{1 + e^{(t-t_p)/W_0}} + P_0 \times (t - t_p) + M_0. \qquad (1)$$

---

[16] The second term in the original equation presented in S. Valenti et al. (2016) is $P_0 \times t$, which is a typo that was confirmed by the corresponding author.

We fit the light curves starting at day 60 (which corresponds to when the evolution is ≈75% of the way to its steepest descent; J. A. Goldberg et al. 2019) to day 150 using the nonlinear least-squares routine `scipy.optimize.curve_fit`, fixing P_0 to be the slope on the ^{56}Ni tail. The derived median and 1σ uncertainty for the plateau duration are $t_p = (81.78 \pm 0.19)$ days for the V-band light curve and $t_p = (82.47 \pm 0.07)$ days for the bolometric light curve, which are consistent with the plateau duration of $t_p = (83.08 \pm 0.08)$ days in M. C. Bersten et al. (2024).

Curiously, the derived slope on the radioactive tail for the V-band light curve corresponds to a decline rate of $P_0 \approx (1.16 \pm 0.08)$ mag per 100 days,[17] slightly higher than the value of ≈0.98 mag per 100 days expected for the typical ^{56}Ni decay. The steepened slope during the nebular phase could be explained by incomplete trapping due to γ-ray leakage, commonly seen in short-plateau SNe IIP with steeper declines, where the progenitors have partially stripped, low-density envelopes (e.g., J. P. Anderson et al. 2014; V. Morozova et al. 2015; B. Paxton et al. 2018; D. Hiramatsu et al. 2021). In accordance with the steeper decline rate, we fit the bolometric light curve with a modified energy deposition rate from J. C. Wheeler et al. (2015):

$$L_{\text{tail}} = L_{\text{decay}}[1 - e^{-(T_0/t)^2}], \tag{2}$$

where

$$L_{\text{decay}} = \frac{M_{\text{Ni}}}{M_\odot}(6.45e^{-t/t_{\text{Ni}}} + 1.45e^{-t/t_{\text{Co}}}) \times 10^{43}\,\text{erg s}^{-1} \tag{3}$$

is the $^{56}\text{Ni}\rightarrow^{56}\text{Co}\rightarrow^{56}\text{Fe}$ decay luminosity given by D. K. Nadyozhin (1994), $t_{\text{Ni}} = 8.8$ days, $t_{\text{Co}} = 111.3$ days, t is the time in days since the explosion, and T_0 is the γ-ray diffusion timescale. Roughly speaking, T_0 indicates the strength of γ-ray trapping within the ejecta. As $T_0 \rightarrow \infty$, the instantaneous heating rate given by Equation (3) is recovered and no leakage occurs (i.e., complete trapping).

Fitting Equation (2) to our bolometric light curve from day 90 to 150 yields a nickel mass of $M_{\text{Ni}} = (0.068 \pm 0.001)\,M_\odot$ and a leakage timescale of $T_0 = 190 \pm 3$ days. The ^{56}Ni mass we derive here is slightly higher than the value of $0.059\,M_\odot$ found by A. Singh et al. (2024), marginally consistent with the $0.071\,M_\odot$ found by E. A. Zimmerman et al. (2024), and notably higher than the $0.04\,M_\odot$ found by T. J. Moriya & A. Singh (2024) or the $0.05\,M_\odot$ found by M. C. Bersten et al. (2024). The discrepancies in the derived M_{Ni} values may be caused by the timescale used to fit the energy deposition rate (e.g., up to ∼110 days in M. C. Bersten et al. 2024 and E. A. Zimmerman et al. 2024), the spectral range used (e.g., UVOIR in A. Singh et al. 2024 and optical only in T. J. Moriya & A. Singh 2024), and procedural differences in calculating bolometric corrections. Other factors such as late-time CSM interaction (A. Singh et al. 2024; G. Folatelli et al. 2025), which may contribute up to 5% of the total luminosity (K. A. Bostroem et al. 2024), could add to the uncertainty of M_{Ni}. Therefore, the derived value here should be viewed as a rough approximation rather than the true yield of SN 2023ixf.

3. Comparison to Light-curve Model Grids

The main goal of this work is to constrain progenitor properties (e.g., envelope mass and progenitor radius), as well as explosion properties (e.g., explosion energy and nickel mass), for SN 2023ixf. Since these intrinsic SN properties are constrained primarily by quantities on the plateau, we only consider phases when CSM interaction no longer dominates the total luminosity during the plateau evolution, which we take to be $t \geqslant 30$ days based on the break in R_{BB} in Figure 2 (although there is evidence for low levels of continued interaction; see K. A. Bostroem et al. 2024 and A. Singh et al. 2024). In the following section, we compare our bolometric light curve to two sets of model grids (D. Hiramatsu et al. 2021; T. J. Moriya et al. 2023), which vary progenitor, CSM, and explosion properties. For simplicity, we evaluate χ^2 values and infer progenitor and explosion properties based on the χ^2 distribution of each model grid used.

3.1. Moriya et al. Accelerated Wind Models

We obtain the large grid of precomputed multifrequency hydrodynamic models from T. J. Moriya et al. (2023). The grid[18] contains 228,016 synthetic light curves simulated using the multigroup radiation hydrodynamics code `STELLA` (S. I. Blinnikov et al. 1998, 2006; S. Blinnikov et al. 2000; S. Blinnikov & E. Sorokina 2004; P. V. Baklanov et al. 2005), based on five RSG progenitor models with initial masses of 10, 12, 14, 16, and 18 $M_\odot$ from T. Sukhbold et al. (2016), and evolved with `KEPLER` (T. A. Weaver et al. 1978). Confined CSM density structures following a β-law wind velocity profile are attached on top of the progenitor models, with varying mass-loss rates, CSM extents, and wind acceleration parameters. The models span a wide range of explosion and CSM parameters, with $E_{\text{exp}} = (0.5 - 5) \times 10^{51}$ erg, $M_{\text{Ni}} = (0.001\text{–}0.3)\,M_\odot$, $\dot{M} = (10^{-5} - 10^{-1})\,M_\odot\ \text{yr}^{-1}$, $R_{\text{CSM}} = (1\text{–}10) \times 10^{14}$ cm, and $\beta = 0.5\text{–}5.0$. More details regarding the setup of the model grid can be found in T. J. Moriya et al. (2023). We present a few of the top models selected via χ^2 minimization in the left panel of Figure 3.

The top models ($\chi^2 \approx 4800$) from the T. J. Moriya et al. (2023) model grid all exhibit the same behavior of overestimating the plateau luminosity and underestimating the tail luminosity, but replicate the plateau duration well. They all share the same progenitor and explosion parameters: an initial mass of $M_{\text{ZAMS}} = 10\,M_\odot$ (or a final mass of $M_{\text{final}} = 9.7\,M_\odot$), a pre-explosion radius of $R = 510\,R_\odot$, an explosion energy of $E_{\text{exp}} = 2 \times 10^{51}$ erg, and a nickel mass of $M_{\text{Ni}} = 0.06\,M_\odot$. Qualitatively, these models behave similarly to those recovered in T. J. Moriya & A. Singh (2024), with the main difference being the derived M_{Ni}, which is likely the result of fitting the bolometric light curve in this work as opposed to fitting the pseudo-bolometric light curve constructed with only optical coverage.

We additionally perform the same χ^2 fits to the plateau phase (30–90 days) and the early nebular phase (90–150 days) independently (not shown). We find that models with $M_{\text{ZAMS}} = 12\,M_\odot$, $E_{\text{exp}} = 1.5 \times 10^{51}$ erg, and $M_{\text{Ni}} <$

---

[17] Note that P_0 here, while qualitatively describing the same portion of the light curve, is not the same as s_3 quoted in M. C. Bersten et al. (2024) and A. Singh et al. (2024), which follows the prescription in J. P. Anderson et al. (2014). If we follow the same procedure, we do recover $s_3 = (1.29 \pm 0.03)$ mag per 100 days using the V-band light curve, which is consistent with A. Singh et al. (2024). M. C. Bersten et al. (2024) inferred $s_3 = (1.71 \pm 0.74)$ mag per 100 days by fitting the bolometric magnitudes.

[18] Accessible at doi:https://datadryad.org/dataset/10.5061/dryad.pnvx0k6sj (T. Moriya et al. 2023).

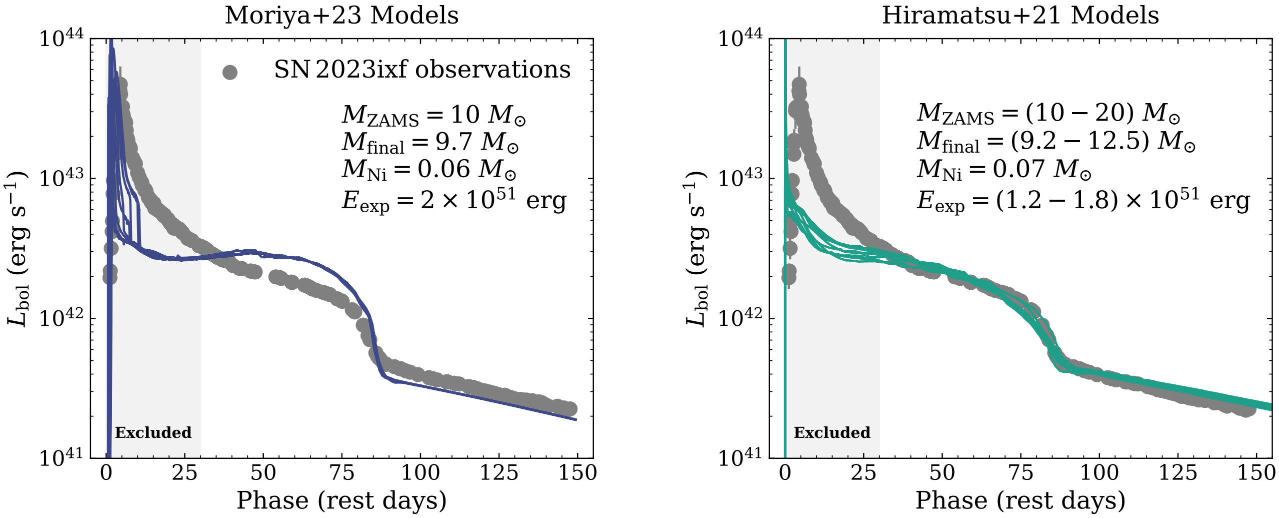

Figure 3. Comparison of our bolometric light curve to models from T. J. Moriya et al. (2023; left) and D. Hiramatsu et al. (2021; right). The regions shaded in light gray indicate epochs excluded from the χ^2 fitting procedure. Here, $M_{\rm final}$ refers to the mass of each corresponding progenitor model at core collapse. The models from T. J. Moriya et al. (2023) match the plateau duration, but systematically overestimate the plateau luminosity and underestimate the tail luminosity. On the other hand, the models from D. Hiramatsu et al. (2021) reproduce the plateau and nebular-phase behaviors of SN 2023ixf well.

$0.01\,M_\odot$ can replicate the plateau behaviors, while models with $M_{\rm ZAMS} = 12\,M_\odot$, $E_{\rm exp} = 5 \times 10^{51}$ erg, and $M_{\rm Ni} = 0.08\,M_\odot$ can replicate the early-nebular-phase behaviors. When these parameter values are combined, however, we find either inflated plateau luminosity or underestimated tail luminosity, with the plateau duration displaced by up to 10 days. Even if we restrict the timescale to 50–120 days to minimize any potential effects of obscured CSM interaction during the plateau and avoid phases on the radioactive tail, where the assumptions of hydrodynamic models begin to break down, we still find that no meaningful combination of $M_{\rm ZAMS}$, $E_{\rm exp}$, and $M_{\rm Ni}$ in the model grid can reproduce properties on the plateau and the radioactive tail simultaneously.

There may be a combination of several reasons why the model grid from T. J. Moriya et al. (2023) is unable to reproduce the plateau and nebular-phase luminosity of SN 2023ixf. Most important of all is perhaps the established relationship between plateau properties and progenitor structures, such as the radius and the hydrogen-rich envelope mass (e.g., D. V. Popov 1993; D. Kasen & S. E. Woosley 2009; L. Dessart et al. 2013; T. J. Moriya et al. 2016). In this vein, the stellar models from T. Sukhbold et al. (2016) may not reflect the true properties of SN 2023ixf's progenitor. In addition, the plateau properties also depend critically on the explosion energy and synthesized nickel mass, as they collectively set the extent of plateau luminosity, which affects the subsequent evolution of the H-recombination front (see Section 4.1). Moreover, the nonuniqueness of light-curve properties as a function of progenitor mass in SNe IIP has been discussed in detail (e.g., L. Dessart & D. J. Hillier 2019; J. A. Goldberg et al. 2019; J. A. Goldberg & L. Bildsten 2020), especially when considering variations in stellar structure due to varied stellar mass loss (e.g., V. Morozova et al. 2015; D. Hiramatsu et al. 2021; L. Dessart et al. 2024).

3.2. *Hiramatsu et al. CSM-free Models*

Motivated by the reasons outlined in Section 3.1, we retrieve the CSM-free model grids from D. Hiramatsu et al. (2021) constructed using Modules for Experiments in Stellar Astrophysics (`MESA`; B. Paxton et al. 2011, 2013, 2015, 2018, 2019; A. S. Jermyn et al. 2023) + `STELLA`, and compare them with our observations in the right panel of Figure 3. The advantages of the models from D. Hiramatsu et al. (2021) are that they survey a wider range of progenitor mass (10–25 $M_\odot$ in increments of 2.5 $M_\odot$) and take various mass-loss efficiencies ($\eta_{\rm wind}$ = 0–3 in increments of 0.1) into consideration over the lifetime of each RSG progenitor. These extra measures result in a more diverse array of progenitor structures prior to explosion compared to those five unique progenitor masses from T. Sukhbold et al. (2016) used in T. J. Moriya et al. (2023). The caveats of these models are that the ranges of $E_{\rm exp} = (0.5 - 2.0) \times 10^{51}$ erg (in increments of 0.5×10^{51} erg) and $M_{\rm Ni} = 0.04, 0.07, 0.1\,M_\odot$ employed are much more restrictive than the models from T. J. Moriya et al. (2023).

After performing the same χ^2 fitting procedure to the bolometric light curve from 30 to 150 days after explosion, we find that lower-mass stars that undergo moderate mass loss and higher-mass stars that undergo intense mass loss can equally reproduce the light-curve behaviors of SN 2023ixf ($\chi^2 \approx$ 300–500). Models with high-mass progenitors ($M_{\rm ZAMS} \gtrsim 15\,M_\odot$) lose >30% of their initial mass, which may be unrealistically high for single RSGs (e.g., E. R. Beasor et al. 2020) undergoing standard stellar evolution, and we will discuss the implications of this later in the paper. Most of these progenitor models also have a larger pre-explosion radius ($R \approx$ 460–820 $R_\odot$) and a lower envelope mass ($M_{\rm H,env} \approx$ 3–5 $M_\odot$) compared to the best-fit models from Section 3.1. We derive a ^{56}Ni mass of 0.07 $M_\odot$ here, which is consistent with $M_{\rm Ni} = 0.068\,M_\odot$ from Section 2.3. The explosion energies of $E_{\rm exp} = 1.2 - 1.8 \times 10^{51}$ erg recovered here are also systematically lower than the $E_{\rm exp} = 2 \times 10^{51}$ erg found in Section 3.1, which correspond to models with lower $M_{\rm final}$ that require lower energies to match observed properties for a given radius (see Section 4.1).

Given that relatively low-mass progenitors with moderate mass loss and high-mass progenitors with enhanced mass loss can both reproduce plateau behaviors, additional constraints must be imposed to further discern the physical origin of SN 2023ixf.

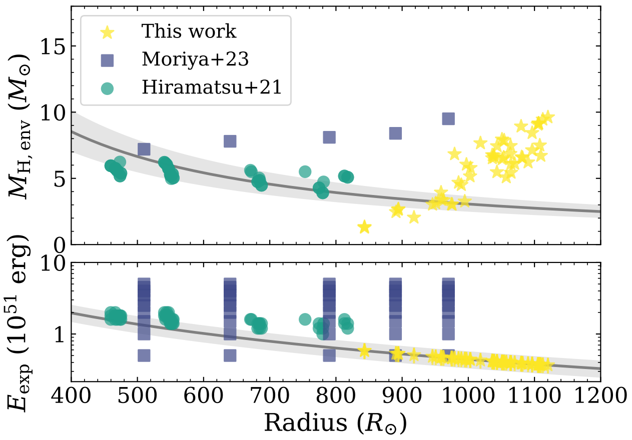

Figure 4. Degeneracy curves for SN 2023ixf recovered from the scaling relations of J. A. Goldberg et al. (2019) as a function of progenitor radius. The gray solid lines indicate the H-rich envelope mass (top panel) and explosion energy (bottom panel) required for a given progenitor radius to match the observed SN properties such as plateau duration and luminosity at day 50. For demonstration purposes, the degeneracy curves were constructed with a nickel mass of $M_{\rm Ni} = 0.068\,M_\odot$. Shaded regions correspond to 1σ bounds that take the intrinsic scatter of the scaling relations and errors on the parameters used into account. We also show models from T. J. Moriya et al. (2023, navy squares; all possible combinations), those from D. Hiramatsu et al. (2021, green circles; top 50 models selected via χ^2 fitting), and our own modeling (yellow stars; models selected via pulsation period).

4. Constraining Progenitor and Light-curve Models with Pulsation Period

4.1. Degeneracy in Type IIP SN Light Curves

An important caveat of the model grid from T. J. Moriya et al. (2023) is the fixed pre-explosion mass–radius relationship of the progenitors. In fact, this caveat applies to any attempt to derive a pre-explosion mass from a grid of progenitor models where each underlying progenitor star exploded is identified with a single progenitor radius at the time of explosion. As shown in J. A. Goldberg et al. (2019) and J. A. Goldberg & L. Bildsten (2020; see also discussions in L. Martinez & M. C. Bersten 2019 and L. Dessart & D. J. Hillier 2019), there exist degeneracies ("a family of explosions") between progenitor radius, ejecta mass, and explosion energy that cannot be lifted with one-to-one mappings of pre-explosion progenitor properties and explosion properties. These degeneracies can be well described by the scaling relations of D. V. Popov (1993), D. Kasen & S. E. Woosley (2009), T. Sukhbold et al. (2016), J. A. Goldberg et al. (2019), and others.

We show the corresponding degeneracy curves for SN 2023ixf using the scaling relations of J. A. Goldberg et al. (2019) in Figure 4 (their Equation (22)), calculated with the bolometric luminosity at day 50 (L_{50}), plateau duration (t_p), and ^{56}Ni mass ($M_{\rm Ni}$), and overplotted with the models from T. J. Moriya et al. (2023) and D. Hiramatsu et al. (2021). Instead of plotting $M_{\rm ej}$, we show the H-rich envelope mass $M_{\rm H,env}$ in Figure 4. The original argument for using $M_{\rm ej}$ to calibrate the scaling relations in J. A. Goldberg et al. (2019) was that their models exhibited strong mixing of hydrogen deep into the interior of the star from self-consistent mixing via the P. C. Duffell (2016) Rayleigh–Taylor instability (RTI) mixing prescription. This resulted in the majority of the ejecta partaking in hydrogen recombination and thus collectively driving the evolution of the SN on the plateau. However, the models in T. J. Moriya et al. (2023; with progenitors from T. Sukhbold et al. 2016), those in D. Hiramatsu et al. (2021), and our own (see the following subsections) contain progenitors that only have little to no hydrogen mixed into the core. Additionally, in partially stripped envelopes, the H-rich envelope mass makes up a smaller fraction of the total ejecta mass. Therefore, the H envelope mass at the time of explosion is the more appropriate choice to use for comparing to scaling relations here, as it drives the bulk evolution of the luminosity during the photospheric phase.

From Figure 4, it is not surprising to see that the best-fitting models from the precomputed grid of T. J. Moriya et al. (2023) are all consistent with a low-mass progenitor with a higher explosion energy, as the $10\,M_\odot$ (with $M_{\rm H,env} = 7.2\,M_\odot$) progenitor model exploded with $E_{\rm exp} = (1.5 - 2) \times 10^{51}$ erg perfectly intersects both degeneracy curves. The same argument goes for the initially high-mass progenitors from D. Hiramatsu et al. (2021) that lose significant amounts of mass and end up with larger radii prior to core collapse, thereby only requiring $E_{\rm exp} \approx 10^{51}$ erg (note as well that these models all have a similar remaining H envelope mass of $\approx$4–7 $M_\odot$, due to the stronger mass-loss prescription adopted in more massive stars). Models that intersect the degeneracy curves are also the best-fitting models selected via χ^2 distributions in Section 3, further supporting the choice of using $M_{\rm H,env}$ instead of $M_{\rm ej}$. The ability of these simple scaling laws in predicting explosion properties highlights the crucial need for independent measurements of the progenitor radius in aiding hydrodynamical modeling of SN IIP light curves.

Another important measurement that may provide an alternative constraint on progenitor and explosion properties is the expansion velocity, or the photospheric velocity, as it encodes information regarding progenitor and explosion properties (i.e., $M_{\rm ej}$, R, and $E_{\rm exp}$). The expansion velocity is typically inferred from the absorption minimum of the Fe II λ5169 line (L. Dessart & D. J. Hillier 2005; O. Pejcha & J. L. Prieto 2015; C. P. Gutiérrez et al. 2017; T. Müller et al. 2017). Several works in the literature (e.g., L. Martinez & M. C. Bersten 2019; W. Ricks & V. V. Dwarkadas 2019; L. Martinez et al. 2020, 2022b) argue that simultaneously fitting the bolometric light curve and photospheric velocity evolution can help estimate the physical properties of SNe II given the significant dispersion and outliers on the observed L–$v_{\rm ph}$ relationship (e.g., O. Pejcha & J. L. Prieto 2015; C. P. Gutiérrez et al. 2017; Ó. Rodríguez et al. 2020). There are also several studies establishing the existence of a "standard candle" relation between L and $v_{\rm ph}$, which was first discovered observationally by M. Hamuy (2003) and explained physically by D. Kasen & S. E. Woosley (2009). This $L \propto v_{\rm ph}^2$ relation (up to a dilution factor that is taken to be a function only of the luminosity; R. V. Wagoner 1981; R. G. Eastman et al. 1996) during the photospheric phase serves as the foundation for the expanding photosphere method for measuring distances to SNe (R. P. Kirshner & J. Kwan 1974), as well as the standardized candle method for SN IIP cosmology (e.g., K. Maguire et al. 2010a; E. F. Olivares et al. 2010; T. de Jaeger et al. 2020; C. Vogl et al. 2024). In this context, other works (e.g., J. A. Goldberg et al. 2019; J. A. Goldberg & L. Bildsten 2020; Q. Fang et al. 2025) have argued against using $v_{\rm ph}$ during the plateau phase as an independent parameter for breaking light-curve degeneracies. Given the significant divide surrounding this topic, we

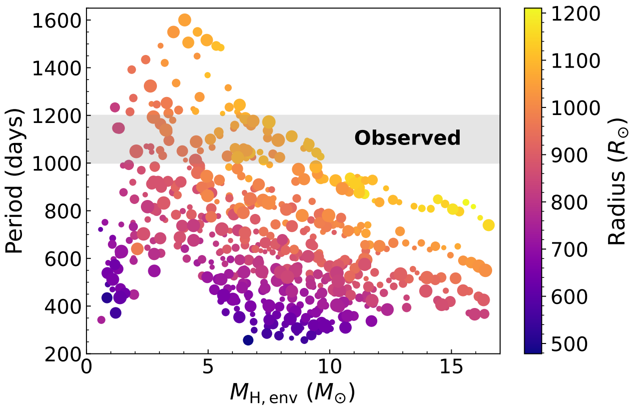

Figure 5. Pulsation period at ≈7000 days before core collapse as a function of the hydrogen envelope mass $M_{\mathrm{H,env}}$ at explosion. Each model is color-coded by the progenitor radius and the size corresponds to the initial mass M_{ZAMS}. The shaded region in gray highlights the models with periods within the range $P = 1000$–1200 days, consistent with the observed IR variability in M. D. Soraisam et al. (2023) and J. E. Jencson et al. (2023). Models that are consistent with the observed variability have $M_{\mathrm{ZAMS}} = 13$–$24\ M_\odot$ and final masses of $M_{\mathrm{final}} \approx 6.5$–$15.46\ M_\odot$ (which correspond to envelope masses of $M_{\mathrm{H,env}} \approx 1.28$–$9.26\ M_\odot$) at the time of core collapse.

focus our discussion only on light-curve degeneracies on the plateau luminosity.

Due to the high circumstellar extinction of SN 2023ixf's progenitor (J. E. Jencson et al. 2023; C. D. Kilpatrick et al. 2023; M. D. Soraisam et al. 2023; S. D. Van Dyk et al. 2024; D. Xiang et al. 2024), the measurement of pre-explosion radius—which may help identify the explosion parameters—is a nontrivial task accompanied by significant uncertainty. In the next section, we seek to remedy our inability to accurately determine the progenitor radius from pre-explosion imaging by creating an additional small grid of `MESA` models with a wide range of progenitor properties, and narrow down viable candidate models via observed variability. We stress here that the mass derived from hydrodynamic modeling reflects the pre-explosion state of the progenitor, and any inference regarding the ZAMS conditions of the progenitor depends sensitively on the physical assumptions (such as mass loss and convective efficiency) adopted in the stellar evolution code.

4.2. *`MESA` Progenitor Models Matching Observed Progenitor Variability*

An important, unique constraint on the nature of SN 2023ixf's progenitor comes from the observed IR variability with a periodicity of $P \approx 1100$ days (J. E. Jencson et al. 2023; C. D. Kilpatrick et al. 2023; M. D. Soraisam et al. 2023). RSG variability has been well studied in galactic and nearby stellar populations (e.g., J. S. Jurcevic et al. 2000; L. L. Kiss et al. 2006; J. R. Percy & V. C. Khatu 2014; C. Conroy et al. 2018; M. D. Soraisam et al. 2018; F. W. Chatys et al. 2019; Y. Ren et al. 2019), with periods typically ranging from a few hundred to a few thousand days with period–luminosity relations characteristic of fundamental-mode and first-overtone radial pulsations. While the pulsation phase may impact the light curves via the ≈10% variation in the progenitor radius at the time of explosion (J. A. Goldberg et al. 2020), RSG pulsation periods are mostly sensitive to the star's luminosity and envelope density (R. Stothers 1969; J. H. Guo & Y. Li 2002; M. Joyce et al. 2020). We thus construct additional models in order to incorporate additional information about the stellar structure provided by the observed progenitor variability.

Using `MESA` revision 23.05.1, we construct nonrotating, solar-metallicity ($Z = 0.02$)[19] models with varying ZAMS masses ($M_{\mathrm{ZAMS}} = 10$–$25\ M_\odot$ in increments of $0.5\ M_\odot$) and convective efficiencies ($\alpha_{\mathrm{MLT}} = 1.5$–3 in increments of 0.5) in the hydrogen-rich envelope. We note that varying α_{MLT} provides additional variation in the stellar radius (R. B. Stothers & C.-W. Chin 1995; P. Massey & K. A. G. Olsen 2003; G. Meynet et al. 2015; J. A. Goldberg et al. 2022a). We adopt `MESA`'s "Dutch" prescription for winds with varying efficiency factors ($\eta_{\mathrm{wind}} = 0$–3 in increments of 0.5), and use modest convective overshooting parameters $f_{\mathrm{ov}} = 0.01$ and $f_{0,\mathrm{ov}} = 0.005$. For reference, a wind efficiency of $\eta_{\mathrm{wind}} = 1$ under the Dutch scheme translates to a mass-loss rate that is ~10 higher than measured values for normal RSG winds ($\dot{M}_{\mathrm{wind}} \lesssim 10^{-5}\ M_\odot\ \mathrm{yr}^{-1}$; e.g., E. R. Beasor et al. 2020). Other inputs are determined following the `12M_pre_ms_to_core_collapse` case of the `MESA` test suite, which is based on the setup described in Section 6 of B. Paxton et al. (2018) and R. Farmer et al. (2016).

To compare the candidate RSG progenitor of SN 2023ixf, which exhibited strong variability with a long baseline period of $P \approx 1100$ days (J. E. Jencson et al. 2023; M. D. Soraisam et al. 2023), we use the the pulsation instrument `GYRE` version 7.2 (R. H. D. Townsend & S. A. Teitler 2013) to identify the period for the fundamental radial ($l = 0$) mode at ≈7000 days prior to the onset of core collapse (which loosely translates to core C burning). `GYRE` is based on a Magnus multiple shooting scheme and provides both adiabatic and nonadiabatic solutions to the linearized pulsation equations for high-resolution structural models produced during the RSG phase. We consider only adiabatic results in this analysis. We plot the period as a function of the hydrogen envelope mass $M_{\mathrm{H,env}}$ and progenitor radius at core collapse in Figure 5, which shows that a low envelope mass ($\lesssim 10\ M_\odot$) and a large progenitor radius ($\gtrsim 800\ R_\odot$) are required to match the observed variability. While model uncertainties on pulsation periods may have an effect on our analysis here, they are largely restricted to resolution effects (Y. Li & M. Joyce 2025) at well under ~10% for RSG variability, and should be captured by the large range of α_{MLT} considered here (M. Joyce et al. 2020). In any case, we do not expect any model uncertainties to exceed or approach the uncertainty of the observed pulsation period.

Another caveat of our model grid, similar to the findings in D. Hiramatsu et al. (2021), is that many low-mass models ($M_{\mathrm{ZAMS}} \lesssim 12.5\ M_\odot$) develop degenerate cores and fail to converge during later burning stages that require off-center ignition (O, Ne, or Si). While excluding these models may introduce some bias to our sample, most of these low-mass progenitors likely will not have the correct physical properties (e.g., a low envelope mass with a larger radius; see Figure 5) required to satisfy the high fundamental-mode pulsation period observed for SN 2023ixf. For reference, the highest pulsation period at the end of core C burning we find for these models is $P \approx 975$ days ($M_{\mathrm{ZAMS}} = 12.5\ M_\odot$, $\eta_{\mathrm{wind}} = 2.0$, and $\alpha_{\mathrm{MLT}} = 1.5$), outside the selection criteria of $P = 1000$–1200

---

[19] S. D. Van Dyk et al. (2024) found that the metallicity at the SN site is compatible with subsolar to supersolar values, but for simplicity here, we only consider solar metallicity.

Table 1
Progenitor and Explosion Properties of Our MESA+STELLA Models

Progenitor Model	$M_{\rm ZAMS}$ ($M_\odot$)	$\eta_{\rm wind}$	$\alpha_{\rm MLT}$	$M_{\rm final}$ ($M_\odot$)	$M_{\rm H,env}$ ($M_\odot$)	R ($R_\odot$)	P (days)	$E_{\rm exp}$ (10^{51} erg)	$M_{\rm ej}$ ($M_\odot$)	$M_{\rm fallback}$ ($M_\odot$)	χ^2
16.5M_eta2.5_alpha2.0	16.5	2.5	2.0	8.53	3.39	959	1094	0.70	6.48	0.40	297.10
17.5M_eta2.5_alpha2.0	17.5	2.5	2.0	8.74	3.26	995	1139	0.66	6.21	0.78	318.37
18.0M_eta2.5_alpha1.5	18.0	2.5	1.5	8.53	3.02	976	1167	0.68	6.05	0.80	597.14
21.0M_eta1.5_alpha1.5	21.0	1.5	1.5	9.95	3.35	962	1131	0.70	6.83	1.25	657.83
18.0M_eta1.5_alpha1.5	18.0	1.5	1.5	8.80	3.04	975	1164	0.68	5.79	1.18	1050.54

Note. Here, $M_{\rm final}$, $M_{\rm H,env}$, and R are the final stellar mass, hydrogen-rich envelope mass, and radius at the time of core collapse; P is the fundamental-mode pulsation period at ≈7000 days before core collapse; and $M_{\rm ej}$ and $M_{\rm fallback}$ are the surviving ejecta mass and fallback mass at the time of shock breakout.

days we impose on period. We therefore discard these models at this stage.

We continue evolving models with pulsation period in the range of $P = 1000$–1200 days through core collapse, then explode the stellar models via thermal bomb energy deposition by modifying the `ccsn_IIp` test suite before handing them off to the radiation hydrodynamics instrument STELLA to create synthetic observables. While exploding progenitor models at the appropriate pulsational phase by injecting a velocity profile proportional to the fundamental-mode eigenfunction as done in J. A. Goldberg et al. (2020) can provide additional constraints, it is outside the scope of this paper and we leave it as an avenue for improved modeling in the future. As first-order estimates for progenitor and explosion properties, we return to the scaling relations to calculate the explosion energy $E_{\rm exp}$ required to match the plateau properties. Since the scaling relations, as well as L_{50} and t_p, have intrinsic uncertainties associated with them, we also capture the 1σ bounds for $E_{\rm exp}$ for a total of three explosion energies for each progenitor model and a total range of $E_{\rm exp} = (0.24 - 0.87) \times 10^{51}$ erg. Due to the large progenitor radii and low envelope masses required to reproduce the observed pulsation period, most of our progenitor models favor relatively low-energy explosions ($E_{\rm exp} < 10^{51}$ erg) in order to simultaneously reproduce the light-curve brightness and duration, in contrast to previous findings (M. C. Bersten et al. 2024; T. J. Moriya & A. Singh 2024; A. Singh et al. 2024). The SN shock propagation is modeled following the prescription of RTI mixing (P. C. Duffell 2016) until near shock breakout, with the final ^{56}Ni scaled to match the total mass of $M_{\rm Ni} = 0.068\ M_\odot$ calculated in Section 2.3. Here, we do not perform any additional mixing (e.g., boxcar) of ^{56}Ni into the hydrogen envelope other than the abundance distribution given by RTI mixing, as it is not clear if and how far ^{56}Ni is mixed beyond the core (see, e.g., D. Kasen & S. E. Woosley 2009; M. C. Bersten et al. 2011; L. Dessart et al. 2013; T. J. Moriya et al. 2016 for the effects of ^{56}Ni mixing on the characteristics of the decay tail).

As this work is concerned with the energetics of SN 2023ixf derived from the plateau, we only explore CSM-free explosion models. We use 800 spatial zones for the SN ejecta and 100 frequency bins to yield convergence in the synthetic bolometric light curves produced by STELLA. Any late-time fallback material produced by reverse shocks from core boundaries interacting with the lowest-velocity inner material is excised via the zero-energy technique described in B. Paxton et al. (2019) and J. A. Goldberg et al. (2019), with an additional standard velocity cut of 500 km s^{-1} at the inner boundary at the handoff between MESA and STELLA. We find that the low explosion energies inferred for our models are not significantly larger than the magnitude of the binding energy of their progenitors at the time of explosion. As such, we observe nonnegligible fallback, with $M_{\rm fallback} \approx 0.5$–$3.6\ M_\odot$. This is also seen in models of some other short-plateau SNe IIP (e.g., R. S. Teja et al. 2024). These materials that do not collapse into the initial compact remnant object could supply additional accretion-powered luminosity that interacts with the ejecta and thereby alter the observed light-curve properties (e.g., J. Dexter & D. Kasen 2013; C. Chan et al. 2018; S. M. Lisakov et al. 2018; T. J. Moriya et al. 2019). We also note that only the innermost ejecta layers experience fallback, so plateau properties mediated by H recombination might be unaffected until the fall from the plateau, with other signatures of fallback accretion possibly manifesting at much later times. Since the proper treatment of late-time fallback and subsequent accretion onto the proto–neutron star in 1D simulations remains an open question, we caution that our models should be viewed as approximations and may not reflect all physical processes at work.

The MESA+GYRE+STELLA inlists used to generate the models in this work are available on Zenodo under an open-source Creative Commons Attribution 4.0 International license: DOI: 10.5281/zenodo.15368365.

4.3. Comparison to Observations

Following the procedure in Section 3, we calculate the χ^2 values of our MESA+STELLA models. We list the progenitor and explosion properties of our top five best-fit models ($\chi^2 \approx 300$–1000) in Table 1 and show the corresponding synthetic bolometric light curves in the top-left panel of Figure 6. The naming convention follows $\langle M_{\rm ZAMS}\rangle$M_eta$\langle\eta_{\rm wind}\rangle$_alpha$\langle\alpha_{\rm MLT}\rangle$_E$\langle E_{\rm exp}\rangle$. With a more detailed modeling that follows the degenerate scaling relations, we recover higher-mass progenitors ($M_{\rm ZAMS} \gtrsim 16.5\ M_\odot$) that shed a significant portion of their hydrogen envelopes to match the plateau behaviors best, similar to our findings in Section 3.2. These models are in good agreement with observations, albeit slightly underluminous during later plateau phases ($t \gtrsim 60$ days). The plateau duration and the radioactive tail, however, are in excellent agreement with observations.

In the bottom-left panel of Figure 6, we compare the expansion velocity of our models to the observed Fe II λ5169 velocity evolution (A. Singh et al. 2024), estimated from the blueshifted absorption trough of the line profile. The line velocity has a systematic uncertainty of ∼500 km s^{-1} dominated by the instrumental resolution (∼10 Å). We show both the photospheric velocity and the Fe II velocity from our best-

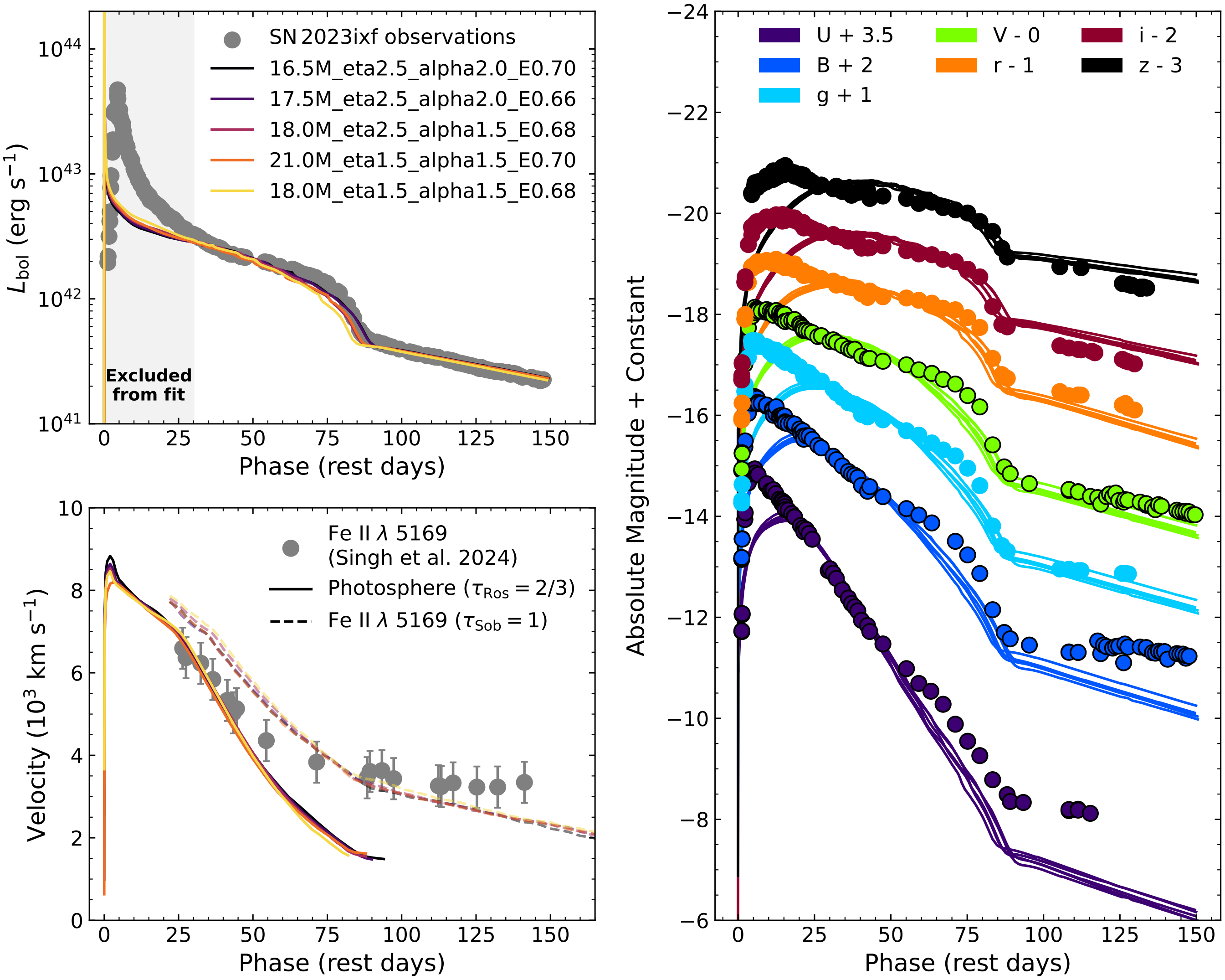

Figure 6. Top left: bolometric light curves of the top five best-fit CSM-free models for SN 2023ixf. The region shaded in light gray indicates epochs excluded from the χ^2 fitting procedure. With the additional constraints from pulsation period and the degeneracy curves, our synthetic light curves recover the plateau properties well. The measured value of $M_{\rm Ni} = 0.068\, M_\odot$ provides excellent agreement with observations on the radioactive tail. Bottom left: the photospheric and Fe II λ5169 velocity estimates of our best-fit models compared to the observed evolution of Fe II λ5169 line velocity from A. Singh et al. (2024). Models that match the plateau luminosity produce nearly identical velocity evolution during the plateau phase. Right: the corresponding optical multiband light curves of the best-fit models.

fit models. The photospheric velocity is calculated at a Rosseland optical depth of $\tau_{\rm Ros} = 2/3$ and the Fe II line velocity is approximated in the Sobolev approximation at a Sobolev optical depth of $\tau_{\rm Sob} = 1$. Note that we are not simultaneously fitting both the bolometric light curve and the observed velocity here; we fit only the luminosity and recover agreement in model velocities.

The photospheric velocities of our best-fit models agree with each other, and give satisfactory matches with observations up to ~45 days before diverging. This is because the photosphere migrates inward in mass coordinates as the ejecta expand, and the Fe II λ5169 line is expected to form exterior to the photosphere (see a detailed discussion in B. Paxton et al. 2018). At later times, the divergence between the line-forming region and the photosphere becomes more pronounced, as the decay of ^{56}Ni and ^{56}Co increases the overall Fe abundance and slows the inward progression of the line-forming region in mass coordinates (V. V. Sobolev 1960; J. I. Castor 1970; D. Mihalas 1978; D. Kasen et al. 2006). Attempts to account for this deviation by raising the explosion energy would cause a mismatch to the luminosity and overestimate the early-time velocity. However, the same models are also underluminous in bluer bands (see right panel in Figure 6), and accounting for the color information may help alleviate the discrepancy in photospheric velocity during the late plateau phase. In contrast, the model Fe II velocities approximated at $\tau_{\rm Sob} = 1$ are systematically higher than observations. This is not concerning, as the precise Sobolev optical depth where the Fe II line is formed is not known, and evaluating the velocity at a higher $\tau_{\rm Sob}$ closer to the location of the photosphere can resolve this discrepancy, as might geometric effects due to deviations from spherical symmetry (D. Vartanyan et al. 2025). Likewise, a lower metallicity that is consistent with the environmental study of SN 2023ixf presented in S. D. Van Dyk et al. (2024) or an asymmetric explosion (Q. Fang et al. 2024; G. Li et al. 2024) can also explain the faster model Fe II velocities. While these models show satisfactory qualitative agreement with the observed velocities, none of our models, including those not shown that provide weaker fits to the bolometric light curve, show exceptional agreement with the entire observed velocity evolution. This highlights the complex physics at play that govern the evolution of SN 2023ixf and the nature of its progenitor and environment.

In the right panel of Figure 6 we show the corresponding optical multiband light curves for the same models, which are constructed by convolving the SEDs returned by `STELLA` with the transmission function of each filter ($UBVgriz_s$) at each time step. The luminosity excess in both the observed bolometric light curve and the multiband light curves, as well as the higher observed photospheric velocity compared to our models at $t \gtrsim 60$ days, could be explained by the presence of a less dense and extended CSM structure (e.g., V. Morozova et al. 2017; A. Singh et al. 2024), which supplies additional energy. In the case of SN 2023ixf, sustained CSM interaction during the plateau phase has been confirmed both photometrically and spectroscopically, with estimated densities of $\sim 10^{-20}$–10^{-16} g cm^{-3} (or mass-loss rates of 10^{-5}–10^{-3} $M_\odot$ yr^{-1} if we assume a steady-state wind) for the material ejected from its RSG progenitor ≈7–33 yr prior to explosion (K. A. Bostroem et al. 2024; A. Singh et al. 2024). It is worth noting that even with this additional CSM interaction, the ejecta is not expected to slow down significantly (L. Dessart et al. 2017). The excess on the radioactive tail in redder bands could be attributed to radiation leaking out from bluer bands, and a more centrally concentrated ^{56}Ni distribution could potentially resolve the discrepancies in colors.

5. Discussion

5.1. Differences Compared to Previous Work

SN 2023ixf has been the object of several investigations since its discovery, ranging from pre-explosion observations of the SN site to properties of the SN itself. The wealth of pre-explosion observations and detailed studies of the early evolution provide constraints on the progenitor that are among the best of any modern SN event. Yet despite these excellent observational constraints, there remains significant disagreement on the star's initial mass, with a wide range of values of $M_{\rm ZAMS} = 8$–$20\,M_\odot$ (e.g., J. E. Jencson et al. 2023; Z. Niu et al. 2023; J. L. Pledger & M. M. Shara 2023; M. D. Soraisam et al. 2023; M. C. Bersten et al. 2024; L. Ferrari et al. 2024; T. J. Moriya & A. Singh 2024; J. M. M. Neustadt et al. 2024; Y.-J. Qin et al. 2024; A. Singh et al. 2024; S. D. Van Dyk et al. 2024; D. Xiang et al. 2024).

Previous hydrodynamical modeling (e.g., M. C. Bersten et al. 2024; T. J. Moriya & A. Singh 2024; A. Singh et al. 2024) has pointed to low H envelope masses, and thus seemed to agree with the lower end of initial mass estimation from some progenitor studies (C. D. Kilpatrick et al. 2023; J. M. M. Neustadt et al. 2024; S. D. Van Dyk et al. 2024; D. Xiang et al. 2024). In contrast, our detailed light-curve modeling indicates that SN 2023ixf does not need to be an energetic explosion of a low-mass progenitor. Instead, a more massive RSG progenitor ($M_{\rm ZAMS} \approx 17$–$21\,M_\odot$) that lost more than half of its ZAMS mass can also reproduce the observed light curve. This work is the first light-curve modeling effort that derives a progenitor mass that is consistent with the higher initial masses estimated from pre-explosion imaging (J. E. Jencson et al. 2023; Z. Niu et al. 2023; M. D. Soraisam et al. 2023; Y.-J. Qin et al. 2024), and is further supported by the independent constraint of the progenitor star's pulsation period.

Both these options—a lower initial mass with less mass loss, as compared to a higher initial mass with more mass loss—can end up at the time of explosion with the right combination of H envelope mass and stellar radius (see the top panel of Figure 4). This is the main reason that a range of different models can adequately approximate the light-curve shape when exploded with the appropriate explosion energy.

It is important to recognize that these model differences are artificial, because they simply depend on the adopted mass-loss prescription, none of whose empirical rates resemble the much lower mass-loss rates of actual RSG winds (e.g., E. R. Beasor et al. 2020, 2023; K. Antoniadis et al. 2024; L. Decin et al. 2024). With more realistic mass-loss rates, single RSGs at all initial masses lose very little mass via steady winds during the RSG phase, so single RSGs should retain most of their H envelopes until the time of explosion (E. R. Beasor et al. 2021). Additionally, as noted by E. R. Beasor et al. (2020), the baseline "Dutch" mass-loss prescription overestimates normal RSG winds by a factor of ∼10, whereas winds with $\eta_{\rm wind}$ values of 1.5–2.5 are even more artificially inflated. Nevertheless, models with extremely strong winds seem to do a good job of yielding a final envelope mass that explains the light-curve shape of SN 2023ixf.

5.2. A Binary Companion Stripping the Envelope?

In the context of RSG evolution, the most plausible way to interpret the agreement of observations with our models that have artificially inflated mass-loss rates is not that the progenitor had a bizarrely strong wind (even though this is how the models are engineered to lose their envelopes). Rather, a much more likely scenario is that the progenitor was in a binary system, and the removal of much of the H envelope was accomplished via stripping by close encounters with its companion star. If the progenitor did in fact have a higher initial mass, as our analysis of the progenitor's pulsation period seems to require, then strong binary mass stripping is essential to achieve the low envelope mass required to explain SN 2023ixf. This is consistent with the growing observational consensus that most massive stars live in binaries (e.g., H. Sana et al. 2012; S. E. de Mink et al. 2013; M. Moe & R. Di Stefano 2017) and with the lack of bright precursor outbursts before SN 2023ixf (Y. Dong et al. 2023; D. Hiramatsu et al. 2023; J. M. M. Neustadt et al. 2024; C. L. Ransome et al. 2024). Some studies find that binary interaction may be the formation channel for only a modest fraction of all SNe IIP (e.g., N. Sravan et al. 2019; A. Ercolino et al. 2024), which would make SN 2023ixf unusual.

Our study requires that a large mass of order 10 $M_\odot$ was removed from the star early in its evolution in order to attain the appropriate properties for the observed pulsation period (see Figure 5). For either Case A or Case B mass transfer, multiple studies predict that the donor stars in these scenarios inevitably end up as either yellow supergiants or blue supergiants, if not completely stripped to become Wolf–Rayet stars (e.g., Y. Götberg et al. 2017; E. Laplace et al. 2020; K. Sen et al. 2022; P. Marchant & J. Bodensteiner 2024). This would seem at odds with the identification of SN 2023ixf's progenitor as an RSG from pre-explosion imaging (e.g., J. E. Jencson et al. 2023; M. D. Soraisam et al. 2023; S. D. Van Dyk et al. 2024), unless the progenitor swelled up to become red in its final years.

Instead, a more suitable scenario for SN 2023ixf is a binary system that has undergone Case C or Case BC mass transfer, which is consistent with simulations of interacting wide massive binaries with a high initial mass ratio (A. Ercolino et al. 2024). We caution, however, that the presence of a nearby companion close to explosion (i.e., the explosion took place during binary interaction or soon after) may modify the geometry of the progenitor, which may violate the spherical symmetry assumed when calculating the pulsation period using `GYRE`. A more detailed analysis of the pulsation period for a nonspherical star may then be necessary to further constrain the progenitor mass. Nevertheless, even without the aid of pulsation period, models with high initial mass and strong envelope mass loss are still contenders for the progenitor of SN 2023ixf, as indicated by our light-curve comparisons in Sections 3.2 and 4. Case BC mass transfer also paints a more self-consistent picture for the dense CSM in the vicinity of the progenitor, where most of the envelope mass is stripped during core He burning and the CSM is formed during later interactions. T. Matsuoka & R. Sawada (2024) found mass-loss rates achieved via binary interactions during the final evolutionary stages of RSG stars that are comparable to values inferred for SN 2023ixf.

Spectropolarimetric data from S. S. Vasylyev et al. (2023), A. Singh et al. (2024), and M. Shrestha et al. (2025) also revealed a continuum polarization level of $\approx$1% one day after discovery, before dropping to $\approx$0.5% and eventually disappearing along with narrow emission-line features over the first $\sim$5–10 days of SN 2023ixf's evolution. This indicates that either the pre-explosion mass loss was highly asymmetric in nature (which is in agreement with the results of high-resolution spectroscopy in the first week after explosion in N. Smith et al. 2023), the shock broke out aspherically (C. D. Matzner et al. 2013; J. A. Goldberg et al. 2022b; A. Singh et al. 2024), or both. A disklike CSM geometry is different from the spherically symmetric mass loss assumed in most models for SN 2023ixf in the literature. It does, however, seem in good agreement with the hypothesis that the progenitor was in an interacting binary system, as noted above. The motion of a nearby companion star, or perhaps a companion embedded in the common envelope of the inflated RSG progenitor, could drive mass ejection concentrated toward the equatorial plane leading up to the time of explosion (e.g., N. Smith & W. D. Arnett 2014; O. Pejcha et al. 2016). In this framework, a CSM structure that consists of a dense, asymmetric disk or torus in conjunction with a low-density, extended wind (N. Smith et al. 2023; S. S. Vasylyev et al. 2023; A. Singh et al. 2024) may be the most plausible configuration for SN 2023ixf.

5.3. Other Possible Mechanisms for Envelope Stripping and CSM Formation

Can some other mass-loss mechanism besides binary mass stripping account for the loss of most of SN 2023ixf's H envelope? Currently, there is no observational evidence for any bright outbursts in SN 2023ixf's progenitor star for the last $\sim$15 yr (Y. Dong et al. 2023; D. Hiramatsu et al. 2023; J. M. M. Neustadt et al. 2024; C. L. Ransome et al. 2024). More importantly, in the case of SN 2023ixf, brief signatures of shock interaction limit the CSM to a total mass of $\lesssim 0.1\,M_\odot$ (K. A. Bostroem et al. 2023a; W. V. Jacobson-Galán et al. 2023), lost in the few years just before core collapse, with a much weaker preceding stellar wind (K. A. Bostroem et al. 2024). The dense CSM has nowhere near enough mass to account for the $\sim 10\,M_\odot$ lost during the star's life, so the removal of the H envelope must have occurred much earlier in the progenitor's evolution. This rules out any eruptive mass-loss mechanism tied to instabilities in the final nuclear burning phases (Ne, O, and Si burning; W. D. Arnett & C. Meakin 2011; N. Smith & W. D. Arnett 2014; S. E. Woosley & A. Heger 2015) or wave driving during those same phases (E. Quataert & J. Shiode 2012; J. H. Shiode et al. 2013; J. H. Shiode & E. Quataert 2014; J. Fuller 2017; S. Wu & J. Fuller 2021; S. C. Wu & J. Fuller 2022).

There have been several suggestions for how to achieve strong RSG mass loss in the literature, involving local super-Eddington luminosities (S. J. Cheng et al. 2024), pulsation-driven superwinds (A. Heger et al. 1997; S.-C. Yoon & M. Cantiello 2010), and turbulent instabilities (A. Chiavassa et al. 2011, 2024; J. A. Goldberg et al. 2022a; J. Fuller & D. Tsuna 2024) that may drive mass-loss rates of order 10^{-5}–$10^{-4}\,M_\odot$ yr^{-1}. To strip such a significant portion of the progenitor's envelope, however, would require these mechanisms to have been sustained for a large fraction of the RSG phase. This is in conflict with observations of normal RSGs, which limit any enhanced mass-loss phases to about 1% of the time during the post-main-sequence phase or less (E. R. Beasor & N. Smith 2022), and where mass-loss rates are observed to be lower for most of the RSG phase (E. R. Beasor et al. 2020, 2023; K. Antoniadis et al. 2024; L. Decin et al. 2024). For the case of SN 2023ixf, these enhanced winds are also problematic because these mechanisms tend to scale with close proximity to the luminosity-to-mass ratio of the progenitor, which monotonically increases as the star evolves up the RSG branch, and as it continually loses more mass. One therefore does not expect these mechanisms to slow down or shut off with a significant H envelope remaining, as observations of SN 2023ixf require. Because of this, it is likely that the envelope mass-loss mechanism was different from that which formed the CSM.

On the other hand, the dense CSM has more direct observational constraints, and is less in conflict with observations of normal RSGs, since it must have been formed in a very brief phase. Are there other mechanisms that could produce the dense CSM in the vicinity of SN 2023ixf's progenitor? While bright outbursts have not been detected, observations do not yet rule out the possibility that the progenitor had faint outbursts on shorter timescales compared to the cadence of these dedicated precursor searches (B. Davies et al. 2022; Y. Dong et al. 2023). Such faint and brief outbursts may contribute to the CSM around the progenitor at the time of explosion. Pulsation-driven superwinds and turbulent mass ejections, while not likely to be the cause for the strong envelope stripping, may still be good candidates for forming the immediate CSM structures around SN 2023ixf's progenitor. When taken together, the combination of pulsation-driven superwinds and convectively levitated envelope materials has also been proposed as a way to create a long-lived "effervescent zone" around the progenitor star (N. Soker 2021, 2023). A stagnant effervescent zone may, however, be in tension with the high outflow velocity in the CSM of SN 2023ixf (N. Smith et al. 2023).

Follow-up observations in the next decade will be crucial for determining whether any additional dense shells of CSM also exist far away from the progenitor of SN 2023ixf, as in the case of several SNe IIP that showed signatures of late-time CSM interaction years after explosion (e.g., K. Maguire et al. 2010b; J. L. Prieto et al. 2012; J. C. Mauerhan et al. 2017; J. E. Andrews & N. Smith 2018; K. E. Weil et al. 2020). Although difficult to prove, binary mass stripping seems to be the most straightforward and self-consistent explanation for the removal of most of SN 2023ixf's envelope and the shaping of the immediate dense CSM, and follow-up observations could similarly reveal any surviving companion.

6. Conclusions

We present extensive follow-up photometric observations of SN 2023ixf in the first year of its evolution. By comparing the bolometric light curve to available grids of hydrodynamical models, we find that the plateau properties can be recovered with drastically varying physical parameters for the SN and its progenitor, owing to previously established degeneracies between explosion and progenitor properties. Motivated by this, we construct additional numerical progenitor and light-curve models. For the first time, we impose an additional constraint drawn from the observed period of the progenitor star's pre-explosion variability. Our results suggest that SN 2023ixf may have originated from the explosion of an initially massive ($M_{\rm ZAMS} \gtrsim 16.5\,M_\odot$) RSG progenitor star, with an explosion energy of $\approx 7 \times 10^{50}$ erg, and a ^{56}Ni production of 0.07 $M_\odot$. Single-star models that agree with the observed variability of ≈1100 days are characterized by a lower than usual envelope mass ($\lesssim 3\,M_\odot$) and a pre-explosion radius $\gtrsim 950\,R_\odot$.

Currently, no isolated single-star models can explain the removal of $\sim 10\,M_\odot$ required to match observations of SN 2023ixf, as observed RSG winds are incapable of accomplishing such a feat. We hypothesize that the RSG progenitor likely experienced a sustained period of intense mass loss that removed the majority of its H-rich envelope, probably due to mass stripping by a binary companion. If binary interaction was indeed the culprit that removed much of the envelope of SN 2023ixf's progenitor, it would likely be in a wide binary system with a high mass ratio in order to end up as an RSG, as theoretical models predict (A. Ercolino et al. 2024).

Future UV observations of the SN site could help detect or constrain the presence of a surviving companion star and delineate a more complete picture of the physical origin of SN 2023ixf. With the commencement of the Vera C. Rubin Observatory Legacy Survey of Space and Time (LSST; Ž. Ivezić et al. 2019) in 2025, high-cadence monitoring of nearby RSG populations may become increasingly common, and we will therefore have more examples of SN progenitors with known pulsation periods. The methodology presented in this work that utilizes RSG variability as an independent constraint may therefore offer an alternative way to break scaling degeneracies in future SN IIP light-curve modeling.

Acknowledgments

We thank Erez A. Zimmerman for providing Swift streak photometry and Hubble Space Telescope spectra that were used in earlier versions of this manuscript, Avinash Singh for supplying Fe II λ5169 line velocity measurements, Mathieu Renzo for helpful discussions and comments, and the anonymous referee for suggestions that helped improve the quality of the manuscript. Computations in this work use high-performance computing resources supported by the University of Arizona TRIF, UITS, and Research, Innovation, and Impact and maintained by the UArizona Research Technologies Department. We respectfully acknowledge that the University of Arizona is on the land and territories of Indigenous peoples. Today, Arizona is home to 22 federally recognized tribes, with Tucson being home to the O'odham and the Yaqui.

J.A.G. is supported by the Flatiron Research Fellowship. The Flatiron Institute is supported by the Simons Foundation. Time-domain research by D.J.S. and team is supported by National Science Foundation (NSF) grants AST-1821987, 1813466, 1908972, and 2108032, and by the Heising-Simons Foundation under grant No. 20201864. K.A.B. is supported by an LSST-DA Catalyst Fellowship; this publication was thus made possible through the support of grant 62192 from the John Templeton Foundation to LSST-DA. S.G. is supported by an STScI Postdoctoral Fellowship. V.A.V. acknowledges support from the NSF through grant AST-2108676. Research by Y.D. is supported by NSF grant AST-2008108.

L.G. and C.P.G. acknowledge financial support from the Spanish Ministerio de Ciencia e Innovación (MCIN); the Agencia Estatal de Investigación 10.13039/501100011033; the European Union Next Generation EU/PRTR funds; the Horizon 2020 Research and Innovation Programme of the European Union; the Secretary of Universities and Research (Government of Catalonia), under the PID2023-151307NB-I00 SNNEXT project; the Marie Skłodowska-Curie and Beatriu de Pinós 2021 BP 00168 program; the 2021-SGR-01270 project; the Centro Superior de Investigaciones Científicas (CSIC) under PIE project 20215AT016; and the program Unidad de Excelencia María de Maeztu CEX2020-001058-M. The work of X.W. is supported by National Natural Science Foundation of China (NSFC grant Nos. 12288102 and 12033003), and the Tencent Xplorer prize.

This paper made use of data from the LCO global network of telescopes through the Supernova Key Project and Global Supernova Project. The LCO group is supported by NSF grants AST-1911151 and AST-1911225. This paper makes use of data from the AAVSO Photometric All-sky Survey, whose funding has been provided by the Robert Martin Ayers Sciences Fund and the NSF (AST-1412587).

Funding for SDSS-III has been provided by the Alfred P. Sloan Foundation, the Participating Institutions, the National Science Foundation, and the U.S. Department of Energy Office of Science. The SDSS-III website is http://www.sdss3.org/. SDSS-III is managed by the Astrophysical Research Consortium for the Participating Institutions of the SDSS-III Collaboration, including the University of Arizona, the Brazilian Participation Group, Brookhaven National Laboratory, Carnegie Mellon University, University of Florida, the French Participation Group, the German Participation Group, Harvard University, the Instituto de Astrofisica de Canarias, the Michigan State/Notre Dame/JINA Participation Group, Johns Hopkins University, Lawrence Berkeley National Laboratory, Max Planck Institute for Astrophysics, Max Planck Institute for Extraterrestrial Physics, New Mexico State University, New York University, Ohio State University, Pennsylvania State University, University of Portsmouth, Princeton University, the Spanish Participation Group, University of Tokyo, University of Utah, Vanderbilt University,

University of Virginia, University of Washington, and Yale University.

Facilities: ADS, LCOGT (Sinistro).

Software: Astropy (Astropy Collaboration et al. 2018), `emcee` (D. Foreman-Mackey et al. 2013), `GYRE` (R. H. D. Townsend & S. A. Teitler 2013), `lcogtsnpipe` (S. Valenti et al. 2016), Matplotlib (J. D. Hunter 2007), `MESA` (B. Paxton et al. 2011, 2013, 2015, 2018, 2019; A. S. Jermyn et al. 2023), NumPy (Harris et al. 2020), `py_mesa_reader` (B. Wolf & J. Schwab 2017), SciPy (P. Virtanen et al. 2020), `STELLA` (S. I. Blinnikov et al. 1998, 2006; S. Blinnikov et al. 2000; S. Blinnikov & E. Sorokina 2004; P. V. Baklanov et al. 2005).

ORCID iDs

Brian Hsu https://orcid.org/0000-0002-9454-1742
Nathan Smith https://orcid.org/0000-0001-5510-2424
Jared A. Goldberg https://orcid.org/0000-0003-1012-3031
K. Azalee Bostroem https://orcid.org/0000-0002-4924-444X
Griffin Hosseinzadeh https://orcid.org/0000-0002-0832-2974
David J. Sand https://orcid.org/0000-0003-4102-380X
Jeniveve Pearson https://orcid.org/0000-0002-0744-0047
Daichi Hiramatsu https://orcid.org/0000-0002-1125-9187
Jennifer E. Andrews https://orcid.org/0000-0003-0123-0062
Emma R. Beasor https://orcid.org/0000-0003-4666-4606
Yize Dong (董一泽) https://orcid.org/0000-0002-7937-6371
Joseph Farah https://orcid.org/0000-0003-4914-5625
Lluís Galbany https://orcid.org/0000-0002-1296-6887
Sebastian Gomez https://orcid.org/0000-0001-6395-6702
Estefania Padilla Gonzalez https://orcid.org/0000-0003-0209-9246
Claudia P. Gutiérrez https://orcid.org/0000-0003-2375-2064
D. Andrew Howell https://orcid.org/0000-0003-4253-656X
Réka Könyves-Tóth https://orcid.org/0000-0002-8770-6764
Curtis McCully https://orcid.org/0000-0001-5807-7893
Megan Newsome https://orcid.org/0000-0001-9570-0584
Manisha Shrestha https://orcid.org/0000-0002-4022-1874
Giacomo Terreran https://orcid.org/0000-0003-0794-5982
V. Ashley Villar https://orcid.org/0000-0002-5814-4061
Xiaofeng Wang https://orcid.org/0000-0002-7334-2357

References

Albareti, F. D., Allende Prieto, C., Almeida, A., et al. 2017, ApJS, 233, 25
Anderson, J. P., González-Gaitán, S., Hamuy, M., et al. 2014, ApJ, 786, 67
Andrews, J. E., Pearson, J., Hosseinzadeh, G., et al. 2024, ApJ, 965, 85
Andrews, J. E., Sand, D. J., Valenti, S., et al. 2019, ApJ, 885, 43
Andrews, J. E., & Smith, N. 2018, MNRAS, 477, 74
Antoniadis, K., Bonanos, A. Z., de Wit, S., et al. 2024, A&A, 686, A88
Arnett, W. D., & Meakin, C. 2011, ApJ, 741, 33
Astropy Collaboration, Price-Whelan, A. M., Sipőcz, B. M., et al. 2018, AJ, 156, 123
Baklanov, P. V., Blinnikov, S. I., & Pavlyuk, N. N. 2005, AstL, 31, 429
Baron, E., Branch, D., Hauschildt, P. H., et al. 2000, ApJ, 545, 444
Beasor, E. R., & Davies, B. 2018, MNRAS, 475, 55
Beasor, E. R., Davies, B., & Smith, N. 2021, ApJ, 922, 55
Beasor, E. R., Davies, B., Smith, N., et al. 2020, MNRAS, 492, 5994
Beasor, E. R., Davies, B., Smith, N., et al. 2023, MNRAS, 524, 2460
Beasor, E. R., & Smith, N. 2022, ApJ, 933, 41
Berger, E., Keating, G. K., Margutti, R., et al. 2023, ApJL, 951, L31
Bersten, M. C., Benvenuto, O., & Hamuy, M. 2011, ApJ, 729, 61
Bersten, M. C., Orellana, M., Folatelli, G., et al. 2024, A&A, 681, L18
Blinnikov, S., Lundqvist, P., Bartunov, O., Nomoto, K., & Iwamoto, K. 2000, ApJ, 532, 1132
Blinnikov, S., & Sorokina, E. 2004, Ap&SS, 290, 13
Blinnikov, S. I., Eastman, R., Bartunov, O. S., Popolitov, V. A., & Woosley, S. E. 1998, ApJ, 496, 454
Blinnikov, S. I., Röpke, F. K., Sorokina, E. I., et al. 2006, A&A, 453, 229
Boian, I., & Groh, J. H. 2019, A&A, 621, A109
Bostroem, K. A., Dessart, L., Hillier, D. J., et al. 2023b, ApJL, 953, L18
Bostroem, K. A., Pearson, J., Shrestha, M., et al. 2023a, ApJL, 956, L5
Bostroem, K. A., Sand, D. J., Dessart, L., et al. 2024, ApJL, 973, L47
Brown, P. J., Dessart, L., Holland, S. T., et al. 2007, ApJ, 659, 1488
Brown, T. M., Baliber, N., Bianco, F. B., et al. 2013, PASP, 125, 1031
Bruch, R. J., Gal-Yam, A., Schulze, S., et al. 2021, ApJ, 912, 46
Bruch, R. J., Gal-Yam, A., Yaron, O., et al. 2023, ApJ, 952, 119
Bullivant, C., Smith, N., Williams, G. G., et al. 2018, MNRAS, 476, 1497
Castor, J. I. 1970, MNRAS, 149, 111
Chan, C., Müller, B., Heger, A., Pakmor, R., & Springel, V. 2018, ApJL, 852, L19
Chandra, P., Chevalier, R. A., Maeda, K., Ray, A. K., & Nayana, A. J. 2024, ApJL, 963, L4
Chatys, F. W., Bedding, T. R., Murphy, S. J., et al. 2019, MNRAS, 487, 4832
Cheng, S. J., Goldberg, J. A., Cantiello, M., et al. 2024, ApJ, 974, 270
Chiavassa, A., Freytag, B., Masseron, T., & Plez, B. 2011, A&A, 535, A22
Chiavassa, A., Kravchenko, K., & Goldberg, J. A. 2024, LRCA, 10, 2
Chugai, N. N. 1991, SvAL, 17, 210
Conroy, C., Strader, J., van Dokkum, P., et al. 2018, ApJ, 864, 111
Davies, B., & Beasor, E. R. 2018, MNRAS, 474, 2116
Davies, B., & Beasor, E. R. 2020, MNRAS, 493, 468
Davies, B., Plez, B., & Petrault, M. 2022, MNRAS, 517, 1483
Decin, L., Richards, A. M. S., Marchant, P., & Sana, H. 2024, A&A, 681, A17
de Jaeger, T., Stahl, B. E., Zheng, W., et al. 2020, MNRAS, 496, 3402
de Mink, S. E., Langer, N., Izzard, R. G., Sana, H., & de Koter, A. 2013, ApJ, 764, 166
Dessart, L. 2025, A&A, 694, A132
Dessart, L., Gutiérrez, C. P., Ercolino, A., Jin, H., & Langer, N. 2024, A&A, 685, A169
Dessart, L., & Hillier, D. J. 2005, A&A, 437, 667
Dessart, L., & Hillier, D. J. 2006, A&A, 447, 691
Dessart, L., & Hillier, D. J. 2008, MNRAS, 383, 57
Dessart, L., & Hillier, D. J. 2019, A&A, 625, A9
Dessart, L., & Hillier, D. J. 2022, A&A, 660, L9
Dessart, L., Hillier, D. J., & Audit, E. 2017, A&A, 605, A83
Dessart, L., Hillier, D. J., Waldman, R., & Livne, E. 2013, MNRAS, 433, 1745
Dessart, L., & Jacobson-Galán, W. V. 2023, A&A, 677, A105
Dexter, J., & Kasen, D. 2013, ApJ, 772, 30
Dong, Y., Sand, D. J., Valenti, S., et al. 2023, ApJ, 957, 28
Dong, Y., Valenti, S., Bostroem, K. A., et al. 2021, ApJ, 906, 56
Duffell, P. C. 2016, ApJ, 821, 76
Eastman, R. G., Schmidt, B. P., & Kirshner, R. 1996, ApJ, 466, 911
Ercolino, A., Jin, H., Langer, N., & Dessart, L. 2024, A&A, 685, A58
Fang, Q., Maeda, K., Kuncarayakti, H., & Nagao, T. 2024, NatAs, 8, 111
Fang, Q., Maeda, K., Ye, H., Moriya, T. J., & Matsumoto, T. 2025, ApJ, 978, 35
Faran, T., Nakar, E., & Poznanski, D. 2018, MNRAS, 473, 513
Farmer, R., Fields, C. E., Petermann, I., et al. 2016, ApJS, 227, 22
Ferrari, L., Folatelli, G., Ertini, K., Kuncarayakti, H., & Andrews, J. E. 2024, A&A, 687, L20
Fitzpatrick, E. L. 1999, PASP, 111, 63
Folatelli, G., Ferrari, L., Ertini, K., Kuncarayakti, H., & Maeda, K. 2025, A&A, 698, A213
Foreman-Mackey, D., Hogg, D. W., Lang, D., & Goodman, J. 2013, PASP, 125, 306
Förster, F., Moriya, T. J., Maureira, J. C., et al. 2018, NatAs, 2, 808
Fransson, C. 1984, A&A, 132, 115
Fuller, J. 2017, MNRAS, 470, 1642
Fuller, J., & Tsuna, D. 2024, OJAp, 7, 47
Gal-Yam, A., Arcavi, I., Ofek, E. O., et al. 2014, Natur, 509, 471
Garnavich, P. M., & Ann, H. B. 1994, AJ, 108, 1002
Gehrels, N., Chincarini, G., Giommi, P., et al. 2004, ApJ, 611, 1005
Goldberg, J. A., & Bildsten, L. 2020, ApJL, 895, L45
Goldberg, J. A., Bildsten, L., & Paxton, B. 2019, ApJ, 879, 3
Goldberg, J. A., Bildsten, L., & Paxton, B. 2020, ApJ, 891, 15
Goldberg, J. A., Jiang, Y.-F., & Bildsten, L. 2022a, ApJ, 929, 156
Goldberg, J. A., Jiang, Y.-F., & Bildsten, L. 2022b, ApJ, 933, 164

Götberg, Y., de Mink, S. E., & Groh, J. H. 2017, A&A, 608, A11
Grefenstette, B. W., Brightman, M., Earnshaw, H. P., Harrison, F. A., & Margutti, R. 2023, ApJL, 952, L3
Groh, J. H. 2014, A&A, 572, L11
Guo, J. H., & Li, Y. 2002, ApJ, 565, 559
Gutiérrez, C. P., Anderson, J. P., Hamuy, M., et al. 2017, ApJ, 850, 89
Hamuy, M. 2003, ApJ, 582, 905
Heger, A., Jeannin, L., Langer, N., & Baraffe, I. 1997, A&A, 327, 224
Harris, C. R., Millman, K. J., van der Walt, S. J., et al. 2020, Natur, 585, 357
Henden, A. A., Templeton, M., Terrell, D., et al. 2016, yCat, II, 336
Hillier, D. J., & Dessart, L. 2019, A&A, 631, A8
Hiramatsu, D., Howell, D. A., Moriya, T. J., et al. 2021, ApJ, 913, 55
Hiramatsu, D., Tsuna, D., Berger, E., et al. 2023, ApJL, 955, L8
Hosseinzadeh, G., Bostroem, K. A., & Gomez, S. 2023a, Light Curve Fitting v0.8.0, Zenodo,
Hosseinzadeh, G., Farah, J., Shrestha, M., et al. 2023b, ApJL, 953, L16
Hosseinzadeh, G., Kilpatrick, C. D., Dong, Y., et al. 2022, ApJ, 935, 31
Hosseinzadeh, G., Valenti, S., McCully, C., et al. 2018, ApJ, 861, 63
Howell, D. A. & Global Supernova Project 2017, AAS Meeting, 230, 318.03
Hunter, J. D. 2007, CSE, 9, 90
Itagaki, K. 2023, TNSTR, 1, 2023
Ivezić, Ž., Kahn, S. M., Tyson, J. A., et al. 2019, ApJ, 873, 111
Jacobson-Galán, W. V., Dessart, L., Davis, K. W., et al. 2024, ApJ, 970, 189
Jacobson-Galán, W. V., Dessart, L., Jones, D. O., et al. 2022, ApJ, 924, 15
Jacobson-Galán, W. V., Dessart, L., Margutti, R., et al. 2023, ApJL, 954, L42
Jencson, J. E., Kasliwal, M. M., Adams, S. M., et al. 2019, ApJ, 886, 40
Jencson, J. E., Pearson, J., Beasor, E. R., et al. 2023, ApJL, 952, L30
Jermyn, A. S., Bauer, E. B., Schwab, J., et al. 2023, ApJS, 265, 15
Joyce, M., Leung, S.-C., Molnár, L., et al. 2020, ApJ, 902, 63
Jurcevic, J. S., Pierce, M. J., & Jacoby, G. H. 2000, MNRAS, 313, 868
Kasen, D., Thomas, R. C., & Nugent, P. 2006, ApJ, 651, 366
Kasen, D., & Woosley, S. E. 2009, ApJ, 703, 2205
Khazov, D., Yaron, O., Gal-Yam, A., et al. 2016, ApJ, 818, 3
Kilpatrick, C. D., Foley, R. J., Jacobson-Galán, W. V., et al. 2023, ApJL, 952, L23
Kirshner, R. P., & Kwan, J. 1974, ApJ, 193, 27
Kirshner, R. P., & Kwan, J. 1975, ApJ, 197, 415
Kiss, L. L., Szabó, G. M., & Bedding, T. R. 2006, MNRAS, 372, 1721
Kozyreva, A., Nakar, E., & Waldman, R. 2019, MNRAS, 483, 1211
Kozyreva, A., Nakar, E., Waldman, R., Blinnikov, S., & Baklanov, P. 2020, MNRAS, 494, 3927
Kumar, A., Dastidar, R., Maund, J. R., Singleton, A. J., & Sun, N.-C. 2025, MNRAS, 538, 659
Landolt, A. U. 1983, AJ, 88, 439
Landolt, A. U. 1992, AJ, 104, 340
Laplace, E., Götberg, Y., de Mink, S. E., Justham, S., & Farmer, R. 2020, A&A, 637, A6
Leavitt, H. S. 1908, AnHar, 60, 87
Li, G., Hu, M., Li, W., et al. 2024, Natur, 627, 754
Li, W., Van Dyk, S. D., Filippenko, A. V., et al. 2006, ApJ, 641, 1060
Li, Y., & Joyce, M. 2025, arXiv:2501.13207
Lisakov, S. M., Dessart, L., Hillier, D. J., Waldman, R., & Livne, E. 2018, MNRAS, 473, 3863
Litvinova, I. I., & Nadezhin, D. K. 1983, Ap&SS, 89, 89
Lundquist, M., O'Meara, J., & Walawender, J. 2023, TNSAN, 160, 1
Maguire, K., Di Carlo, E., Smartt, S. J., et al. 2010b, MNRAS, 404, 981
Maguire, K., Kotak, R., Smartt, S. J., et al. 2010a, MNRAS, 403, L11
Marchant, P., & Bodensteiner, J. 2024, ARA&A, 62, 21
Martinez, L., & Bersten, M. C. 2019, A&A, 629, A124
Martinez, L., Bersten, M. C., Anderson, J. P., et al. 2020, A&A, 642, A143
Martinez, L., Bersten, M. C., Anderson, J. P., et al. 2022a, A&A, 660, A40
Martinez, L., Bersten, M. C., Anderson, J. P., et al. 2022b, A&A, 660, A41
Martinez, L., Bersten, M. C., Folatelli, G., Orellana, M., & Ertini, K. 2024, A&A, 683, A154
Massey, P., & Olsen, K. A. G. 2003, AJ, 126, 2867
Matsuoka, T., & Sawada, R. 2024, ApJ, 963, 105
Matthews, D., Margutti, R., AJ, N., et al. 2023, TNSAN, 180, 1
Matzner, C. D., Levin, Y., & Ro, S. 2013, ApJ, 779, 60
Mauerhan, J. C., Van Dyk, S. D., Johansson, J., et al. 2017, ApJ, 834, 118
Mauron, N., & Josselin, E. 2011, A&A, 526, A156
Meynet, G., Chomienne, V., Ekström, S., et al. 2015, A&A, 575, A60
Mihalas, D. 1978, Stellar Atmospheres (San Francisco, CA: W. H. Freeman & Co.)
Moe, M., & Di Stefano, R. 2017, ApJS, 230, 15
Moriya, T., Subrayan, B., Milisavljevic, D., & Blinnikov, S. 2023, Data for: Synthetic red supergiant explosion model grid for systematic characterization of Type II supernovae, Dryad,
Moriya, T. J., Müller, B., Chan, C., Heger, A., & Blinnikov, S. I. 2019, ApJ, 880, 21
Moriya, T. J., Pruzhinskaya, M. V., Ergon, M., & Blinnikov, S. I. 2016, MNRAS, 455, 423
Moriya, T. J., & Singh, A. 2024, PASJ, 76, 1050
Moriya, T. J., Subrayan, B. M., Milisavljevic, D., & Blinnikov, S. I. 2023, PASJ, 75, 634
Morozova, V., Piro, A. L., Renzo, M., et al. 2015, ApJ, 814, 63
Morozova, V., Piro, A. L., & Valenti, S. 2017, ApJ, 838, 28
Morozova, V., Piro, A. L., & Valenti, S. 2018, ApJ, 858, 15
Müller, T., Prieto, J. L., Pejcha, O., & Clocchiatti, A. 2017, ApJ, 841, 127
Nadyozhin, D. K. 1994, ApJS, 92, 527
Neustadt, J. M. M., Kochanek, C. S., & Smith, M. R. 2024, MNRAS, 527, 5366
Niemela, V. S., Ruiz, M. T., & Phillips, M. M. 1985, ApJ, 289, 52
Niu, Z., Sun, N.-C., Maund, J. R., et al. 2023, ApJL, 955, L15
Olivares, E. F., Hamuy, M., Pignata, G., et al. 2010, ApJ, 715, 833
Panjkov, S., Auchettl, K., Shappee, B. J., et al. 2024, PASA, 41, e059
Paxton, B., Bildsten, L., Dotter, A., et al. 2011, ApJS, 192, 3
Paxton, B., Cantiello, M., Arras, P., et al. 2013, ApJS, 208, 4
Paxton, B., Marchant, P., Schwab, J., et al. 2015, ApJS, 220, 15
Paxton, B., Schwab, J., Bauer, E. B., et al. 2018, ApJS, 234, 34
Paxton, B., Smolec, R., Schwab, J., et al. 2019, ApJS, 243, 10
Pearson, J., Hosseinzadeh, G., Sand, D. J., et al. 2023, ApJ, 945, 107
Pejcha, O., Metzger, B. D., & Tomida, K. 2016, MNRAS, 461, 2527
Pejcha, O., & Prieto, J. L. 2015, ApJ, 799, 215
Percy, J. R., & Khatu, V. C. 2014, JAVSO, 42, 1
Perley, D. A., Gal-Yam, A., Irani, I., & Zimmerman, E. 2023, TNSAN, 119, 1
Pledger, J. L., & Shara, M. M. 2023, ApJL, 953, L14
Popov, D. V. 1993, ApJ, 414, 712
Prieto, J. L., Lee, J. C., Drake, A. J., et al. 2012, ApJ, 745, 70
Qin, Y.-J., Zhang, K., Bloom, J., et al. 2024, MNRAS, 534, 271
Quataert, E., & Shiode, J. 2012, MNRAS, 423, L92
Quimby, R. M., Wheeler, J. C., Höflich, P., et al. 2007, ApJ, 666, 1093
Ransome, C. L., Villar, V. A., Tartaglia, A., et al. 2024, ApJ, 965, 93
Ren, Y., Jiang, B.-W., Yang, M., & Gao, J. 2019, ApJS, 241, 35
Ricks, W., & Dwarkadas, V. V. 2019, ApJ, 880, 59
Riess, A. G., Macri, L. M., Hoffmann, S. L., et al. 2016, ApJ, 826, 56
Rodríguez, Ó., Pignata, G., Anderson, J. P., et al. 2020, MNRAS, 494, 5882
Roming, P. W. A., Kennedy, T. E., Mason, K. O., et al. 2005, SSRv, 120, 95
Sana, H., de Mink, S. E., de Koter, A., et al. 2012, Sci, 337, 444
Schlafly, E. F., & Finkbeiner, D. P. 2011, ApJ, 737, 103
Sen, K., Langer, N., Marchant, P., et al. 2022, A&A, 659, A98
Shigeyama, T., & Nomoto, K. 1990, ApJ, 360, 242
Shiode, J. H., & Quataert, E. 2014, ApJ, 780, 96
Shiode, J. H., Quataert, E., Cantiello, M., & Bildsten, L. 2013, MNRAS, 430, 1736
Shivvers, I., Groh, J. H., Mauerhan, J. C., et al. 2015, ApJ, 806, 213
Shrestha, M., Bostroem, K. A., Sand, D. J., et al. 2024b, ApJL, 972, L15
Shrestha, M., DeSoto, S., Sand, D. J., et al. 2025, ApJL, 982, L32
Shrestha, M., Pearson, J., Wyatt, S., et al. 2024a, ApJ, 961, 247
Singh, A., Teja, R. S., Moriya, T. J., et al. 2024, ApJ, 975, 132
Smartt, S. J. 2009, ARA&A, 47, 63
Smartt, S. J. 2015, PASA, 32, e016
Smith, N. 2014, ARA&A, 52, 487
Smith, N., & Arnett, W. D. 2014, ApJ, 785, 82
Smith, N., Li, W., Filippenko, A. V., & Chornock, R. 2011, MNRAS, 412, 1522
Smith, N., Mauerhan, J. C., Cenko, S. B., et al. 2015, MNRAS, 449, 1876
Smith, N., Pearson, J., Sand, D. J., et al. 2023, ApJ, 956, 46
Sobolev, V. V. 1960, Moving Envelopes of Stars (Cambridge, MA: Harvard Univ. Press)
Soker, N. 2021, ApJ, 906, 1
Soker, N. 2023, RAA, 23, 081002
Soraisam, M. D., Bildsten, L., Drout, M. R., et al. 2018, ApJ, 859, 73
Soraisam, M. D., Szalai, T., Van Dyk, S. D., et al. 2023, ApJ, 957, 64
Sravan, N., Marchant, P., & Kalogera, V. 2019, ApJ, 885, 130
Stothers, R. 1969, ApJ, 156, 541
Stothers, R. B., & Chin, C.-W. 1995, ApJ, 440, 297
Sukhbold, T., Ertl, T., Woosley, S. E., Brown, J. M., & Janka, H. T. 2016, ApJ, 821, 38
Tartaglia, L., Sand, D. J., Groh, J. H., et al. 2021, ApJ, 907, 52

Teja, R. S., Goldberg, J. A., Sahu, D. K., et al. 2024, ApJ, 974, 44
Teja, R. S., Singh, A., Basu, J., et al. 2023, ApJL, 954, L12
Townsend, R. H. D., & Teitler, S. A. 2013, MNRAS, 435, 3406
Utrobin, V. P., & Chugai, N. N. 2005, A&A, 441, 271
Valenti, S., Howell, D. A., Stritzinger, M. D., et al. 2016, MNRAS, 459, 3939
Van Dyk, S. D., Bostroem, K. A., Zheng, W., et al. 2023, MNRAS, 524, 2186
Van Dyk, S. D., Cenko, S. B., Poznanski, D., et al. 2012, ApJ, 756, 131
Van Dyk, S. D., Li, W., & Filippenko, A. V. 2003, PASP, 115, 1289
Van Dyk, S. D., Srinivasan, S., Andrews, J. E., et al. 2024, ApJ, 968, 27
Vartanyan, D., Tsang, B. T. H., Kasen, D., et al. 2025, ApJ, 982, 9
Vasylyev, S. S., Yang, Y., Filippenko, A. V., et al. 2023, ApJL, 955, L37
Virtanen, P., Gommers, R., Oliphant, T. E., et al. 2020, NatMe, 17, 261
Vogl, C., Taubenberger, S., Csörnyei, G., et al. 2024, arXiv:2411.04968
Wagoner, R. V. 1981, ApJL, 250, L65
Weaver, T. A., Zimmerman, G. B., & Woosley, S. E. 1978, ApJ, 225, 1021
Weil, K. E., Fesen, R. A., Patnaude, D. J., & Milisavljevic, D. 2020, ApJ, 900, 11
Wheeler, J. C., Johnson, V., & Clocchiatti, A. 2015, MNRAS, 450, 1295
Wolf, B., & Schwab, J. 2017, wmwolf/py_mesa_reader: Interact with MESA Output v0.3.0 Zenodo,
Woosley, S. E., & Heger, A. 2015, ApJ, 810, 34
Woosley, S. E., & Weaver, T. A. 1986, ARA&A, 24, 205
Wu, S., & Fuller, J. 2021, ApJ, 906, 3
Wu, S. C., & Fuller, J. 2022, ApJ, 930, 119
Xiang, D., Mo, J., Wang, L., et al. 2024, SCPMA, 67, 219514
Yamanaka, M., Fujii, M., & Nagayama, T. 2023, PASJ, 75, L27
Yaron, O., Perley, D. A., Gal-Yam, A., et al. 2017, NatPh, 13, 510
Yoon, S.-C., & Cantiello, M. 2010, ApJL, 717, L62
Zhang, J., Lin, H., Wang, X., et al. 2023, SciBu, 68, 2548
Zheng, W., Dessart, L., Filippenko, A. V., et al. 2025, ApJ, 988, 61
Zimmerman, E. A., Irani, I., Chen, P., et al. 2024, Natur, 627, 759